Physics of the Earth and Planetary Interiors 353 (2024) 107216

Contents lists available at ScienceDirect

Physics of the Earth and Planetary Interiors

journal homepage: www.elsevier.com/locate/pepi

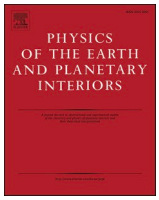

Enigmatic mixture of magnetite magnetofossils and diagenetic greigite as the magnetic carriers of the Early Miocene lacustrine sediments from the Most Basin in Central Europe

Hakan Ucar [a,b,*], Gunther Kletetschka [a,c], Ramon Egli [d], Karel Mach [e], Michael S. Petronis [f], Hana Grison [g], Stephanie Scheidt [h], Petr Schnabl [b], Simon Kdyr [a,b]

[a] Faculty of Science, Charles University, Prague, Czech Republic
[b] Institute of Geology, The Czech Academy of Sciences, Prague, Czech Republic
[c] Geophysical Institute, University of Alaska Fairbanks, AK, USA
[d] Central Institute for Meteorology and Geodynamics, Vienna, Austria
[e] North Bohemian Mines, j.s.c., Bilina, Czech Republic
[f] Environmental Geology, Natural Resources Management Department, New Mexico Highlands University, Las Vegas, NM, USA
[g] Institute of Geophysics, The Czech Academy of Sciences, Prague, Czech Republic
[h] Institute of Geology and Mineralogy, University of Cologne, Zülpicher Str. 49a, 50674 Cologne, Germany

ARTICLE INFO

Keywords:
Early Miocene
Lacustrine sediments
Central Europe
Greigite
Magnetite
Magnetofossils
Rock magnetism
Magnetostratigraphy

ABSTRACT

The Early Miocene lacustrine sediments of the Most Basin in the Czech Republic preserve a European continental paleoenvironmental archive. A number of paleoenvironmental and magnetostratigraphic studies have been carried out on sediment cores from boreholes due to ongoing coal mining in the basin. However, the magnetic carriers of the studied sediments have not been identified clearly. Here, we present a detailed paleo-rock magnetic study from the Burdigalian sediments near the Bilina mining area, Most Basin. The studied clay sediments cover the period of local lakes and a basin-wide lake above the main coal seam. Our results suggest that the magnetic carriers of the studied section in the Most Basin are mixtures of authigenic greigite and magnetite magnetofossils with overlapping magnetic signatures. Greigite is formed by migration of pore water through the sediment column, where iron from siderite grains reacts with these fluids with limited H_2S, which then favors greigite precipitation. The co-existence of greigite and magnetite indicates a partial dissolution of magnetofossils due to H_2S deficiency. Diagenetic greigite has been problematic in paleomagnetic studies due to an unknown time lag between the depositional remanence and the chemical remanent magnetization (CRM). A ghost polarity interval reveals that greigite acquired at least ~45 kyr delayed CRM. The revealed timing of remanence acquisition brings a new perspective to the chronostratigraphic structure of the Most Basin.

1. Introduction

The Most Basin is an 870 km^2 large substructure of the Eger Graben (Rajchl et al., 2009) located in north-western Czech Republic, Central Europe (Figs. 1a and b). The Early Miocene lacustrine sedimentary infill of the Most Basin is a well-preserved European continental paleoenvironmental archive (Matys Grygar and Mach, 2013; Mach et al., 2014; Matys Grygar et al., 2014, 2017a, 2017b, 2019) that was deposited through the onset and during the Miocene Climatic Optimum (MCO, 16.9–14.7 Ma; Kochhann et al., 2016) (Fig. 1c). Sediments of the Most Basin have been studied for >150 years due to ongoing coal mining. Beside characterizations of the environmental and climatic conditions, magnetostratigraphic studies (Matys Grygar et al., 2014, 2017a, 2017b, 2019, 2021) have been conducted in the basin. Those studies mainly aim on age determinations and correlating sediment cores from different boreholes that span the magnetic polarity zones from C5Dr.2r (18.007 Ma; Ogg, 2020) to C5Cn.1n (16.261 Ma; Kochhann et al., 2016) (Fig. 1c). Despite these generally accepted results, the magnetic carriers of the studied sediments have not been identified clearly with a comprehensive rock magnetic investigation. The only attempt to identify the magnetic carriers was made by Matys Grygar et al. (2014) who based their findings on the S-ratio and reported a mixture of low,

* Corresponding author at: Faculty of Science, Charles University, Prague, Czech Republic.
E-mail address: ucarh@natur.cuni.cz (H. Ucar).

https://doi.org/10.1016/j.pepi.2024.107216
Received 27 June 2023; Received in revised form 4 June 2024; Accepted 4 June 2024
Available online 6 June 2024

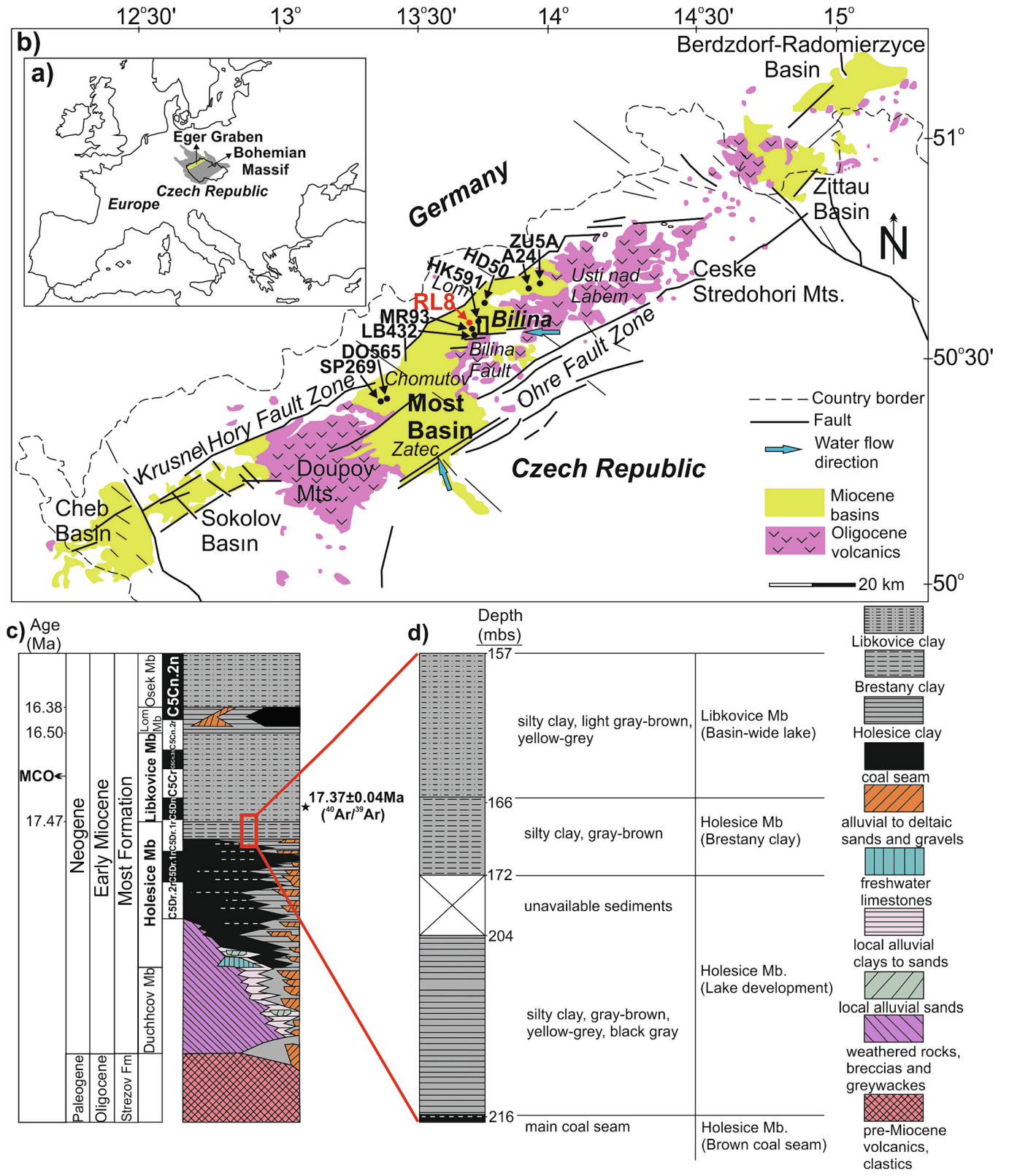

Fig. 1. Location of the study area in (a) Central Europe and Bohemian Massif. Geological map of the Eger Graben in (b) shows the location (solid circles) of the drill cores RL8 (this study, shown in red), HK591 (Matys Grygar et al., 2014, 2017a, 2017b, 2019), ZU5A (Matys Grygar et al., 2017b), A24 (Matys Grygar et al., 2017b), DO565 (Matys Grygar et al., 2019), MR93 (Matys Grygar et al., 2021), LB432 (Matys Grygar et al., 2021) in the Most Basin (modified after Rajchl et al., 2008, 2009; Matys Grygar and Mach, 2013; Mach et al., 2021). Bilina mine is shown in black rectangle. (c) Stratigraphical units and magnetostratigraphy of the Most Basin (modified after Mach et al., 2014, 2021; Matys Grygar et al., 2014, 2019). The time scale is from Matys Grygar et al. (2021) according to the geomagnetic polarity time scale (GPTS) 2020 (Kochhann et al., 2016; Ogg, 2020). Fm: Formation, Mb: Member. (d) Lithological units of the studied cores in RL8 borehole (red rectangle in (c)). mbs: meters below surface. (For interpretation of the references to color in this figure legend, the reader is referred to the web version of this article.)

medium, and high coercivity magnetic minerals (e.g., magnetite, maghemite, and hematite). In particular, the presence of coal seams, preservation of plant fossils (Matys Grygar and Mach, 2013), the dark color of the Most Basin sediments (Mach et al., 2014, 2021; Matys Grygar and Mach, 2013; Matys Grygar et al., 2017b) and the occurrence of greigite within more than a 100 m thick strata in the other Miocene subbasins (Sokolov and Cheb basins, and Chomutov area in Fig. 1b; Krs et al., 1990, 1991, 1992, 1993) of the Eger Graben caution against the possibility that diagenetic iron sulfides could be part of the mineral magnetic assemblage. Thus, from a paleomagnetic point of view, the question of the reliability of the magnetic signals used for magnetic polarity stratigraphy in the Most Basin is not conclusively resolved. This is important because the time lag between acquisition of the primary depositional remanent magnetization (DRM) and the secondary chemical remanent magnetization (CRM) could affect the interpretation of the paleomagnetic records. This issue has been reported in a large number of studies, especially when greigite is involved (e.g., Snowball and Thompson, 1990; Roberts, 1995; Snowball, 1997a; Liu et al., 2004; Demory et al., 2005; Rowan et al., 2009; Roberts et al., 2011; Fu et al., 2015; Nowaczyk et al., 2021). Greigite (Fe_3S_4) is a ferrimagnetic iron sulfide mineral with an inverse spinel crystal structure in which sulfur atoms replace oxygens in magnetite (Fe_3O_4) in a close-packed arrangement (Hoffmann, 1992; Dekkers et al., 2000; Chang et al., 2008; Roberts et al., 2011). Diagenetic greigite is a common recorder of Earth's magnetic field in freshwater sediments (Snowball and Thompson, 1990; Roberts et al., 1996; Torii et al., 1996; Snowball, 1997a) and has been reported frequently in Miocene lake sediments around the world (Babinszki et al., 2007; Vasiliev et al., 2007; Nowaczyk et al., 2012; Chang et al., 2014; Fu et al., 2015; Scheidt et al., 2017; Mandic et al., 2019; Márton et al., 2022). As a precursor to pyrite (FeS_2), greigite may form during early diagenesis (Roberts et al., 2011) and gives rise to a paleomagnetic signal that is equivalent to that acquired by detrital magnetic particles. On the other hand, substantial evidence exists for remagnetization of sediments resulting from later diagenetic greigite formation (Sagnotti et al., 2005). Thus, a CRM recorded by diagenetic iron sulfides in reducing environments can preserve younger paleomagnetic directions than the surrounding sediment by 10's to 100's of kyr (Rowan et al., 2009). Therefore, knowledge of magnetic carriers, chemical stability, age of magnetization, and their ability to preserve a geologically stable remanent magnetization is important for both magnetostratigraphic and paleoenvironmental studies.

Here, we present a detailed paleomagnetic and rock magnetic study of a Most Basin sediment core section to identify the magnetic carriers and to understand the mechanism and timing of the remanence acquisition.

2. Geology of the Most Basin

The Most Basin formed during the Tertiary as part of the Eger Graben (Rajchl et al., 2009). The Early Miocene Most Formation in the Bilina area is a 150–400 m thick sequence of monotonous, macrofossil-barren fluvio-deltaic and lacustrine clastics overlying a lignite seam with coal and clayey coal, and fluvial to deltaic clastic sediments (Fig. 1c; Rajchl et al., 2008; Matys Grygar and Mach, 2013; Matys Grygar et al., 2014). During the main peat swamp period, the basin was mostly supplied by water and clastics from the Zatec River, which later changed its course from the Zatec delta to the Bilina area (Fig. 1b; Rajchl et al., 2008; Matys Grygar and Mach, 2013). Flat peat-forming swamps changed into temporary lakes during periodical flood episodes of wet climate conditions (Mach et al., 2014). Finer-grained mudstones (Fig. 1c; Holesice clay, middle Holesice Member) just above the coal seam (Fig. 1c; lower Holesice Member) are occasionally laminated (Matys Grygar and Mach, 2013) and were deposited in local lake phases (Matys Grygar et al., 2014). Lacustrine clastic strata just above the coal seam compacted the underlying peat producing vertical accommodation space for further fluvial clastics (Matys Grygar et al., 2017b and references therein). Above these sediments, an additional deltaic deposit formed near Bilina. The rivers mixed clastic sediments derived from the Palaeozoic and Cretaceous sediments of the Bohemian Massif and Oligocene volcanic rocks (Matys Grygar and Mach, 2013; Matys Grygar et al., 2014). The Bilina delta has a heterolithic composition made from laminated mudstones, siltstones, or fine to coarse sands (Fig. 1c; Matys Grygar and Mach, 2013; Mach et al., 2014; Matys Grygar et al., 2017a, 2017b). The Brestany clay (thickness up to 15 m), which is kaolinite-rich fine mudstone with occasional siderite cementation, and common plant fossils, occurs at the top of the Holesice Member in the Bilina area, immediately above the uppermost Bilina delta heteroliths (Fig. 1c; Matys Grygar and Mach, 2013; Matys Grygar et al., 2017b). The Brestany clays represent a lake expansion phase (Mach et al., 2021). This unit is overlain by monotonous lacustrine grayish to brownish mudstones (Libkovice Member). These are the thickest member of the Miocene infill (Fig. 1c; Matys Grygar and Mach, 2013; Matys Grygar et al., 2014, 2021). Mach et al. (2021) reported a $^{40}Ar/^{39}Ar$ date for magmatic biotite from an ash layer in the Libkovice Member as 17.37 ± 0.04 Ma (Fig. 1c). The Libkovice Member was deposited in a perennial basin-wide lake (Matys Grygar et al., 2014). Subsequent coalescence of dispersed lakes occurred with increased water level resulting in the first basin-wide freshwater lake (Matys Grygar et al., 2017a). Northwest Europe experienced an increased mean annual precipitation from ca. 17.8 Ma to the Miocene maximum at ca. 17.0 Ma (Matys Grygar et al., 2017b). The basin-wide lake in the Most Basin, thus, formed during these conditions of enhanced precipitation. The Libkovice (or Bilina; Mach et al., 2014) paleolake could have had an area of 1000 km^2 between ~17.5 Ma and 16.5 Ma (Matys Grygar et al., 2019) during the MCO onset in the latest Early Miocene and is overlain by the Lom and Osek members (Fig. 1c; Mach et al., 2014; Matys Grygar et al., 2014, 2017b). The Most Basin was hydrologically open and overfilled, with no evidence of dry periods (Mach et al., 2021). For example, even during peat-forming periods, the water inflow into the basin was in equilibrium with the outflow (Mach et al., 2021).

3. Materials and methods

3.1. Sediment material and sampling

Sediment cores in RL8 borehole (256 m depth) were taken using a rotary drilling system with wireline extraction near the opencast mine in Bilina town of the Czech Republic (50.56°N, 13.63°E; Fig. 1b) by the PKÚ state enterprise for hydrogeological research of the main coal seam waters. The cores were not oriented azimuthally. A total of 27 m of sediment were recovered in 1-m core subsections between 157 and 172 m and 204–216 m depths (Fig. 1d). Sediment cores between 172 and 204 m were not available for investigation due to other research purposes. The cores obtained between 204 and 216 m correspond to the Holesice clay (middle Holesice Member) of the Most Formation, while those between 166 and 172 m correspond to the Brestany clay in the uppermost Holesice Member (Fig. 1d). The sediments between 157 and 166 m are from the Libkovice Member (Fig. 1d).

Overall, the sediments lack macrofossils yet there are signs of lacustrine life with two kinds of microscopic trace fossils (ichnofossils) (Mach et al., 2021). *Planolites montanus* (Mikuláš et al., 2003) occur as tube-like structures with a diameter of 0.5–2 mm and are interpreted as marks left by small invertebrates that lived in the lake bottom sediment (Mach et al., 2021). Abundant thin sulfidic (pyritic) hairy fibers "fossilized bioelectric wires" of *Trichichnus* (Kędzierski et al., 2015) are products of anaerobic bacterial activity in redox conditions (Mach et al., 2021). This sulfidic occurrence is a typical feature of the sediment cores. Fresh sediments are greenish gray and turn brownish gray within a few days due to surficial oxidation. This color change likely indicates that sulfides are not only concentrated in the form of the "bioelectric wires" but are also finely dispersed throughout the clay matrix. To minimize oxidation and preserve the natural remanent magnetization (NRM) of

the sediments until subsampling, the cores were covered with polyethylene foil and stored in a sunless and cool cellar (Supplementary Fig. S1).

Before core opening the individual core sections were placed horizontally on a table and compacted on both sides with wooden boards on a vice. The cores were split in half with a ceramic knife and discrete subsampling was carried out by pushing plastic sample boxes (standard plastic boxes with an internal volume of 7 cm^3) into the sediment with an average spacing of 6.7 cm. The pushing method only deflects the magnetic remanence by <5% (<2.5°; Ucar et al., 2021). A total of 400 oriented paleomagnetic samples resulted from the available core material; downcore direction was used for sample orientation. Deformed core parts caused by drilling operation have been detected visually, especially on the cores between 209 m and 211 m, and samples from this interval show odd orientations in low-field anisotropy of magnetic susceptibility (AMS) measurements (Yang et al., 2019).

For high and low-temperature magnetic susceptibility ($\chi(T)$) and magnetic hysteresis and back-field demagnetization measurements ~0.5 g and ~0.2 g powdered samples were used, respectively. For optical and geochemical analyses, approximately 5 g of sediment from each one-meter core section was sieved using 150 μm, 75 μm, and 45 μm plastic meshes. The finest fractions (<45 μm) were homogenized in distilled water in a plastic container and were extracted magnetically using a neodymium magnet enclosed in a heavy duty ziploc plastic bag.

3.2. Optical and geochemical analyses

X-ray fluorescence (XRF) data were collected from all discrete samples with a 60 s measurement time using an Olympus Vanta XRF analyzer equipped with a 50 kV workstation at the Institute of Hydrogeology, Engineering Geology and Applied Geophysics, Charles University. Carbon coated magnetically extracted grains were imaged using a Tescan Vega scanning electron microscope (SEM) (operated at 15 kV) with back-scattered electron (BSE) and secondary electron (SE) detectors and were analyzed using energy dispersive spectroscopy (EDS) (X-Max 50 and Ultim Max 65 from Oxford Instruments) attached to the SEM at the Institute of Petrology and Structural Geology, Charles University and the Institute of Geology, the Czech Academy of Sciences. The atomic ratio values (at.%) were calculated from the average of several EDS analyses on each grain and are given with their standard deviations. The magnetic extracts and bulk sediment samples were analyzed by X-ray diffraction (XRD) using an X'Pert Pro X-ray diffractometer (PANalytical, Netherlands) at a scanning speed of 0.05°/s, with a 2θ range from 3 to 60° at the Institute of Geochemistry, Mineralogy and Mineral Resources, Charles University.

3.3. Rock magnetic and paleomagnetic analyses

AMS measurements were performed on all samples using an automatic 3D rotator on an MFK1-FA Kappabridge (AGICO, Brno, Czech Republic) operating at 200 A/m applied field and 976 Hz frequency. AMS mean susceptibility values were used as the low-field magnetic susceptibility (χ_{lf}). The frequency dependence of magnetic susceptibility was obtained from measurements at 976 Hz and 15,616 Hz in a 200 A/m applied field using the same system. The frequency dependence parameter (χ_{FD}) was calculated using the formula of Dearing et al. (1996) and expressed in percentage. Note that the percentages provided by Dearing et al. (1996) refer to the MS2 Bartington sensor. This difference has been considered here. High and low-temperature $\chi(T)$ curves were measured using a CS4 and CS-L apparatus attached to the MFK1-FA Kappabridge. The temperature increased at 14°/min rate, between −194 °C and 700 °C with a constant 200 A/m applied field. High-temperature repeated cycles were obtained at 50 °C steps up to 700 °C with intervening cooling to room temperature. All heating/cooling experiments were conducted in an argon atmosphere to limit oxidation.

Hysteresis loop and stepwise back-field demagnetization measurements were performed on 20 samples using a vibrating sample magnetometer (VSM) EV9 (MicroSence, Massachusetts, USA) in a 1 T maximum field at room temperature at the Laboratory of Rock Magnetism, Institute of Geophysics, the Czech Academy of Sciences, Prague. Hysteresis measurement of one sample was performed after heating the sample to 700 °C and cooling it to room temperature using the MFK1-FA system. Easy VSM software (MicroSense LLC) was used to determine hysteresis parameters after high field (>400 mT) slope correction. The shape factor (σ_{hys}) of hysteresis loops proposed by Fabian (2003) was calculated using the HystLab 1.1.2 software (Paterson et al., 2018). The coercivity of remanence (B_{cr}) was determined from backfield demagnetization curves in fields up to 300 mT.

First order reversal curve (FORC) measurements of sample HB161–15 were performed with a Lake Shore Cryotronics 8600 VSM at the laboratory of material magnetism of GeoSphere Austria, using the following protocol parameters: 0.4 mT field step size (701 curves), maximum coercivity ($B_{c,max}$) = 140 mT, lower limit of bias field ($B_{u,min}$) = −49.8 mT, upper limit of bias field ($B_{u,max}$) = +80.2 mT, and saturation field (B_{sat}) = 350 mT. A stepwise approach to the reversal field (B_r) (Wagner et al., 2021) was used to ensure a precise field control (better than 0.05 mT) and the avoidance of measurement artifacts along the left limit of the FORC space. Due to the extreme weakness of the ferrimagnetic signal and a strong paramagnetic overprint (saturation magnetization to maximum magnetization ratio $M_s/M_{max} = 0.005$), 18 identical FORC sequences have been acquired, for a total measurement time of ~718 h, to obtain a sufficient signal-to-noise ratio for further processing. Results have been stacked with VARIFORC v5.0 (Egli, 2013; https://zenodo.org/record/7953336) and processed using the following parameters (see Egli, 2021, for definitions): $s_0 = 12$ (smoothing factor at the origin), $\lambda = 0.18$ (smoothing factor increase rate), $s_{cr} = 6$ (vertical smoothing factor limit across the central ridge), $s_d = 6$ (smoothing factor limit at zero applied field ($B = 0$)), $s_r = 6$ (smoothing factor limit at $B = -B_r = B_{cr}$).

NRMs of all samples were measured using a 2G Enterprises Model 755 superconducting rock magnetometer with integrated alternating field (AF) demagnetizing unit. AF demagnetization experiments involved 15 steps up to a peak field of 100 mT. The characteristic remanent magnetization (ChRM) directions were determined by principal component analysis (PCA) (Kirschvink, 1980) on Zijderveld diagram (Zijderveld, 1967) using the Remasoft 3.0 software (AGICO, Chadima and Hrouda, 2006) with at least 4 continuous demagnetization data points trending towards the origin. The fitting was not anchored to the origin. Following the methods of McFadden and Reid (1982), we used the inclination values from "n" number of specimens to calculate a mean inclination and a dispersion estimate (k) for each magnetic polarity zone, which then allowed the calculation of the α_{95} confidence ellipse about the mean inclination value.

An anhysteretic remanent magnetization (ARM) was imparted on all samples using the anhysteretic magnetizer mode (PAM1) of a LDA5 AF demagnetizer (AGICO, Brno, Czech Republic) with the same steps as NRM demagnetization up to 100 mT with a uniaxial 50 μT steady direct (DC) bias field. AF demagnetization of ARM was performed using the AF demagnetizer mode of the LDA5 system with the same demagnetization steps. ARM susceptibility (χ_{ARM}) was calculated by normalizing ARM with the applied DC field 39.79 A/m (50 μT). Subsequently, an isothermal remanent magnetization (IRM) was imparted with 38 DC field steps up to 2 T using an MMPM10 pulse magnetizer (Magnetic Measurements, Lancashire, UK). Coercivity components were obtained from unmixing of IRM acquisition data using MAX UnMix web application (Maxbauer et al., 2016). AF demagnetization of IRM was performed using the LDA5 system with the same steps as NRM and ARM demagnetization. A second IRM was imparted with a 2 T DC field (SIRM)

and then a 0.3 T DC back-field for S-ratio ($S_{-0.3T}$) determination (Bloemendal et al., 1992). Sample magnetizations were measured after each step using a JR-6A spinner magnetometer (AGICO, Brno, Czech Republic) equipped with a Helmholtz coil system. All of the above-mentioned measurements, except VSM measurements, were performed at the Laboratory of Paleomagnetism, Institute of Geology, Czech Academy of Sciences, Pruhonice.

4. Results and interpretation

4.1. Optical and geochemical analyses

SEM images of magnetic extracts reveal different phases of iron sulfides with sizes <1 μm. The sulfides in Figs. 2a and b occur in framboidal and irregular aggregates which are both typical growth forms of greigite and pyrite (Roberts et al., 2011). Greigite grains generally occur

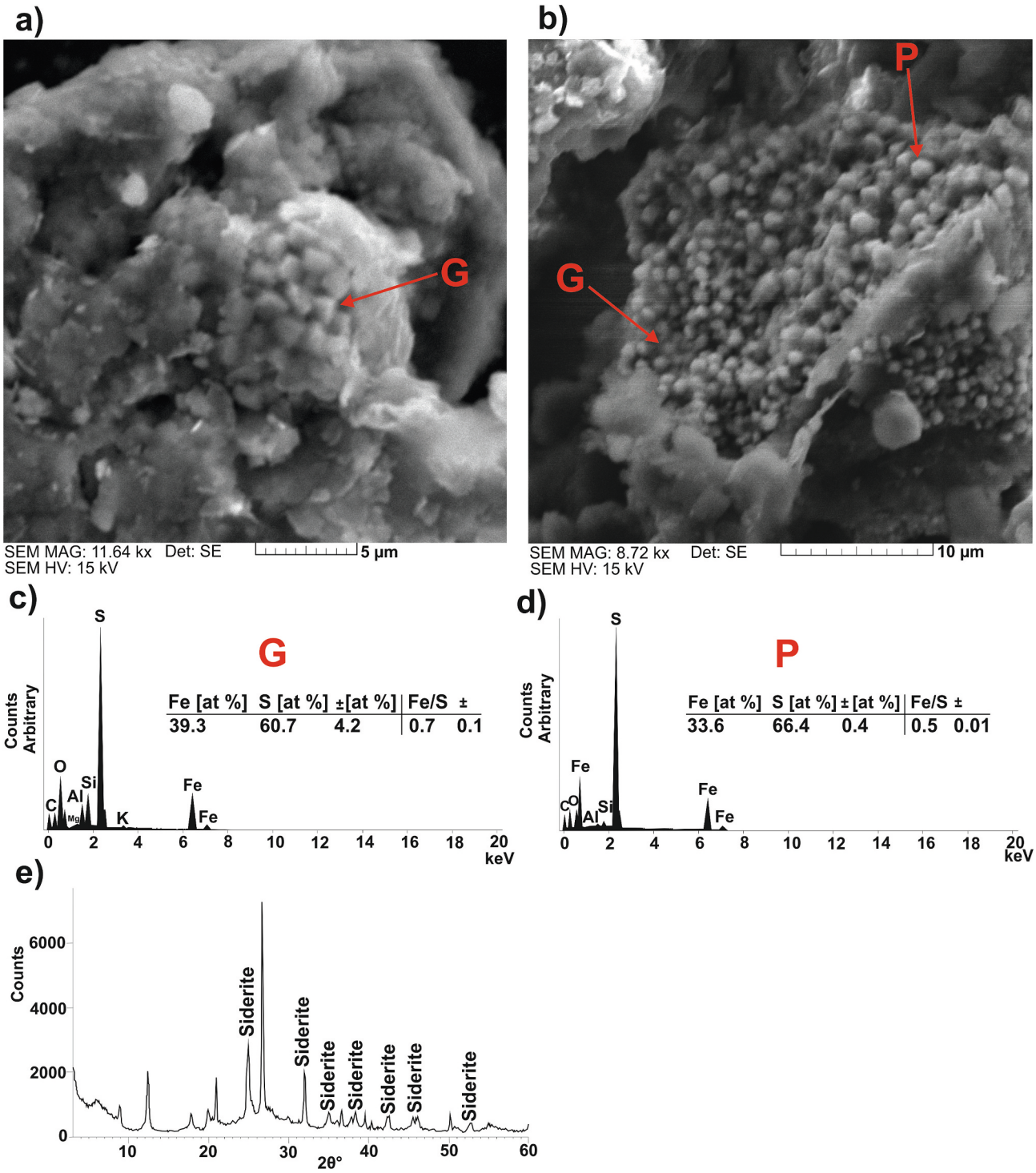

Fig. 2. SEM images of (a) framboidal aggregate of greigite grains (G) from samples between 157 m and 212 m depth, and (b) irregular aggregates of a mixture of greigite (G) and pyrite (P) grains from samples between 213 m and 216 m depth. SE: secondary electrons, BSE: backscattered electrons. (c, d) EDS analyses of G and P, respectively. (e) XRD pattern of the analyzed samples. See section 4.1 for a detailed explanation.

with sizes <1 μm and have a darker contrast in SEM images, while pyrite grains are larger (Jiang et al., 2001; Roberts and Weaver, 2005; Vasiliev et al., 2007; Roberts et al., 2011; Chen et al., 2021). Also, greigite grains with 43% Fe and 57% S differs from pyrite grains with 33% Fe and 67% S (Fu et al., 2015). The finer and darker grains in Figs. 2a and b have 39.3% Fe and 60.7% S (±4.2%) (Fig. 2c) indicating greigite. The coarser and brighter grains in Fig. 2b have 33.6% Fe and 66.4% S (±0.4%) (Fig. 2d) indicating pyrite. The Fe/S ratios for pyrite grains are 0.5 ± 0.01 (Fig. 2d) while greigite grains display values around 0.7 ± 0.1 (Fig. 2c), which is closer to the ratio of greigite (0.75) but higher than that of pyrite (0.5) (Roberts et al., 2011; Chen et al., 2021). Greigite and pyrite grains often occur next to each other to give mixed analyses (Chen et al., 2021). Iron sulfide minerals can also be distinguished by their distinct morphologies: greigite grains tend to be octahedral and occur in isolation as small or framboidal aggregates (Roberts and Weaver, 2005; Vasiliev et al., 2007; Roberts et al., 2011). The octahedral morphology is visible in framboidal greigite aggregate in Fig. 2a. Overall, analyses indicate greigite grains in samples from depths between 157 m and 212 m and a mixture of greigite and pyrite grains in samples from depths between 213 m and 216 m. A mixed iron oxide (possibly magnetite) and fine greigite (sub-μm) composition has also been detected in all depth intervals (Supplementary Fig. S2).

XRD analyses of bulk sediment material in Fig. 2e indicate siderite (see section 5.2 for discussion). Iron sulfides and other ferrimagnetic minerals could not be detected due to the mineral detection limit of XRD analysis (at least 5%; Roberts et al., 2011).

4.2. Bulk rock magnetic analyses

Irreversible heating and cooling $\chi(T)$ curves in Fig. 3a indicate thermal alteration of the initial magnetic minerals. This irreversible behavior is typical of iron sulfides and happens due to the thermal breakdown upon heating to temperatures above 200–350 °C (Snowball and Thompson, 1990; Krs et al., 1992; Fassbinder and Stanjek, 1994; Dekkers et al., 2000; Roberts et al., 2011; Fu et al., 2015). The large χ_{lf} increase during heating (>2 orders of magnitude), is caused by the conversion of paramagnetic iron sulfides (e.g., pyrite) into iron oxides (e.g., magnetite and hematite). The release of H_2S during this reaction was evidenced by the characteristic "rotten egg" smell between 250 °C and 400 °C. On further heating above 450 °C, the rotten egg smell was

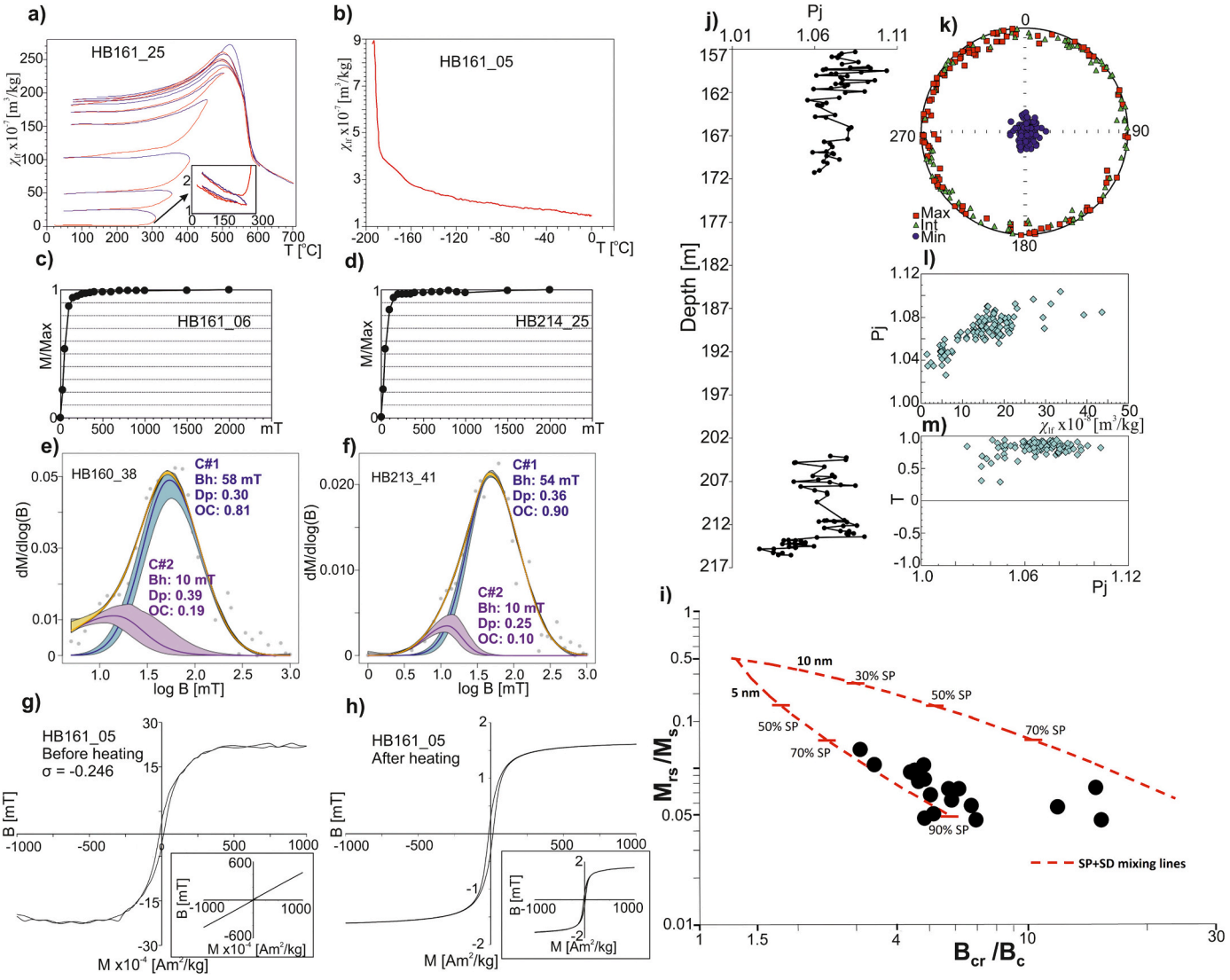

Fig. 3. (a-b) Representative thermomagnetic curves. Red (blue) curves represent heating (cooling). The heating curve below 300 °C is enlarged in the inserted small figure. (c-d) IRM acquisition curves, with (e-f) corresponding IRM unmixing results. (g-h) Hysteresis curve before and after heating to 700 °C. The inserted small figure in (g-h) represents hysteresis curve before removal of the paramagnetic contribution. (i) Day diagram showing M_{rs}/M_s vs. B_{cr}/B_c. (j) P_j vs. depth. (k) Stereographic projection of AMS principal axes. (l) Relation between P_j and χ_{lf}. (m) T vs. P_j.

replaced by a sharp burning smell due to oxidation of organic matter at high temperatures. The samples converted into a coal-like dark black material after the measurements. A yellowish dust of sulfur condensates was observed in the part of the sample tube where the temperature is cooler while brownish moisture formed below (higher temperature) since sulfur turns into a reddish color liquid and gains more viscosity upon heating. Similar behavior were reported in published studies (Spender et al., 1972; Krs et al., 1992; Duan et al., 2017).

The low temperature $\chi(T)$ curve in Fig. 3b contains a faint trace of the Verwey transition (Özdemir et al., 1993) at ~ −165 °C, indicative of the presence of fine-grained magnetite. The origin of the sharp drop below ~ −185 °C is likely caused by the evaporation of paramagnetic liquid oxygen. Greigite does not undergo any low temperature transition (Spender et al., 1972; Dekkers et al., 2000; Chang et al., 2008; Roberts et al., 2011) and is therefore not identifiable in $\chi(T)$ measurements.

The AMS fabric is dominated by paramagnetic minerals. The corrected anisotropy degree (P_j) values of AMS range between 1.02–1.10 and are positively correlated with χ_{lf} that range between 1.4 and 43 × 10^{-8} m^3/kg (Figs. 3j, l and 4h). Overall low P_j values are typical of unconsolidated sediments (Snowball et al., 2019). The shape parameter (T) ranges between 0.35 and 0.95, and the T-P_j plot (Jelinek, 1981) indicate oblate ellipsoids (Fig. 3 m) (Hrouda, 1982; Tarling and Hrouda, 1993). Magnetic fabric directions in most of the samples are characterized by a shallow maximum ($k_1 = 2.2°$) and intermediate ($k_2 = 0.4°$) axes, and steep minimum axes ($k_3 = 87.8°$) (Fig. 3 k). This fabric is compatible with compaction, since k_1 and k_3 are parallel and perpendicular to the bedding plane, respectively (Tarling and Hrouda, 1993; Sier et al., 2017). Similar normal AMS fabric has been reported in fine greigite-bearing marine sediments from New Zealand (Rowan and Roberts, 2006), where it is dominated by paramagnetic clay minerals rather than by greigite (Roberts et al., 2011). These results indicate a non-disturbed magnetic fabric (Duan et al., 2017). k_3 inclinations in some depth intervals show deviations from a perfectly horizontal bedding (see AMS data for rejected samples in Supplementary Fig. S3) (Tarling and Hrouda, 1993).

The dominance of soft magnetic carriers such as magnetite and greigite to saturation remanence (M_{rs}) is indicated by $S_{-0.3T}$ values between 0.93 and 0.98 expressing a saturation of the IRM acquisition curves to 93–98% at 300 mT (Figs. 3c, d and 4e). However, due to full saturation of IRM acquisition curves only between 500 and 700 mT low quantities of magnetic minerals with intermediate coercivity may also be present. IRM component analysis yields evidence for two components. The main component C#1 of the samples carries 81–90% of the total IRM (OC) and is characterized by median coercivity values (Bh) of 54 mT to 58 mT and a dispersion parameter (Dp) between 0.30 and 0.35 (Figs. 3e and f). This coercivity range may indicate different magnetic minerals including magnetite, titanomagnetite, and greigite (Scheidt et al., 2017 and references therein). The Dp value corresponds roughly to the logarithmic standard deviation of the coercivity distribution that is influenced by many factors such as grain sizes, grain shapes and oxidation states of magnetic minerals (Egli, 2004a). Since SEM analyses and $\chi(T)$ measurements demonstrate the presence of greigite and magnetite, it is likely that C#1 consists of different magnetic components with undistinguishable Bh and Dp values. The second component C#2 is a low-coercivity component that might represent ultrafine grains (Egli, 2004b) or deviations of the major IRM component from a lognormal coercivity distribution (Chang et al., 2014).

M_s and M_{rs} values range between 4 and 26 × 10^{-4} Am^2/kg and 0.3–3.3 × 10^{-4} Am^2/kg, respectively (Figs. 4a and b), while B_c and B_{cr} values are comprised between 26 and 63 mT and 3–14 mT, respectively (Figs. 4c and d). Corresponding M_{rs}/M_s and B_{cr}/B_c values range between 0.04 and 0.13 and 3–14, respectively (Fig. 3i). Difference between the hysteresis parameters before (M_{rs} = 2.7 × 10^{-4} Am^2/kg, M_s = 2.6 × 10^{-3} Am^2/kg, B_{cr} = 63.3 mT, B_c = 14.1 mT, M_{rs}/M_s = 0.1, B_{cr}/B_c = 4.4) and after heating (M_{rs} = 3.1 × 10^{-1} Am^2/kg, M_s = 1.6 Am^2/kg, B_{cr} = 29 mT, B_c = 15 mT, M_{rs}/M_s = 0.19, B_{cr}/B_c = 1.9) a sample indicate an increase in the ferrimagnetic content, which supports the oxidation of paramagnetic minerals to iron oxides upon heating during high-temperature $\chi(T)$ measurements. Hysteresis parameters in the Day diagram (Day et al., 1977) fall on 5 nm and 10 nm superparamagnetic and single domain (SP + SD) mixing lines (Dunlop, 2002; Roberts et al., 2006, 2018), respectively (Fig. 3i). This result seems to be supported by typical values of σ_{hys} of about −0.25 (Fig. 3 g) that also indicate a mixed SP/SD composition (Fabian, 2003). However, the Day plot as well as σ_{hys} parameter are meant to be applied to magnetite bearing samples and not to multi-component magnetic mineral compositions (Fabian, 2003; Roberts et al., 2019), and must therefore be interpreted with caution. Nevertheless, there are comparative values in literature. The Day diagram presented by Scheidt et al. (2021) for natural magnetite-bearing samples containing magnetofossils and partially interspersed with greigite has a distribution similar to the values in this study, with B_{cr} values comprised between 47 and 67 mT and M_{rs}/M_s values between 0.24 and 0.35 within the greigite influenced part. In contrast, greigite bearing sediments in Scheidt et al. (2017) and Roberts et al. (2011) indicate SD to SP grain size in the Day plot with M_{rs}/M_s of up to ~0.6 and ~0.8, respectively. However, Roberts et al. (2011) also report comparable B_{cr} values of 46–62 mT for natural greigite-bearing samples, while Dekkers and Schoonen (1996) found values as low as 37 mT for hydrothermally synthesized greigite consisting of mixture of SP and SD or small pseudo-single-domain (PSD) grains. The latter study also highlights an extensive overlap of the hysteresis parameters of greigite with those of magnetite. Thus, the range of B_{cr} and M_{rs}/M_s values of our samples fits well into greigite-bearing samples that include magnetite, as also suggested by the low-temperature $\chi(T)$ curve and SEM analyses.

ARM and SIRM values range between 0.1 and 3.8 × 10^{-6} Am^2/kg and 2–86 × 10^{-6} Am^2/kg, respectively (Figs. 4f and g). The χ_{ARM}/IRM ratio is a sensitive proxy for the domain state of remanence carriers. Non-interacting SD magnetite particles are characterized by values between ~2 mm/A and ~5 mm/A (Egli and Lowrie, 2002; Egli, 2004a), compared to <0.25 mm/A for particles whose size exceeds the stable SD range. Magnetostatic interactions between SD particles drastically reduce χ_{ARM}/IRM already at small concentrations, e.g., by a factor of 5 for a 1% magnetite dispersion (Egli, 2006). χ_{ARM}/IRM values in Fig. 4i are comprised between ~1.0 and ~1.9 mm/A: these values fall within the gap between non-interacting SD and non-SD particles pointing either to a mixture of domain states, or to SD particles affected by magnetostatic interactions. This range of values is intermediate between χ_{ARM}/IRM values reported for fully preserved magnetofossil-bearing sediments (2–4 mm/A) and magnetite-depleted, greigite-bearing layers (~0.5 mm/A) (Fu et al., 2008). Its overlap with χ_{ARM}/IRM values of sediments that have undergone reductive diagenesis while still preserving magnetofossil signatures (Egli, 2004a) suggests a magnetic signature dominated by mixtures of magnetofossils and authigenic greigite. Finally, the increasing trend in the 157–172 m depth interval, which is not reflected by other domain state sensitive parameters such as M_{rs}/M_s, might be explained by an increasing degree of magnetite preservation. The lower depth interval, on the other hand, does not show any significant trend.

Frequency-dependent magnetic susceptibility is a sensitive indicator for the presents of fine SP grains (Chang et al., 2009; Hrouda and Pokorný, 2011). The χ_{FD} has a non-monotonic dependence on grain size distributions, with maximum values of up to 20% for narrow distributions peaking at the lower SD stability range (~20 nm for magnetite and greigite), and lower values for finer or larger grains, respectively (Worm, 1998). The χ_{FD} values of the analyzed sediments in this study range between 0.6% and 7.0% (Fig. 4j), indicating a highly variable content of SP particles. The combination of relatively large χ_{ARM}/IRM values, which points to a significant contribution of SD particles, and M_{rs}/M_s values <0.1 for most samples further supports the presence of a SP contribution.

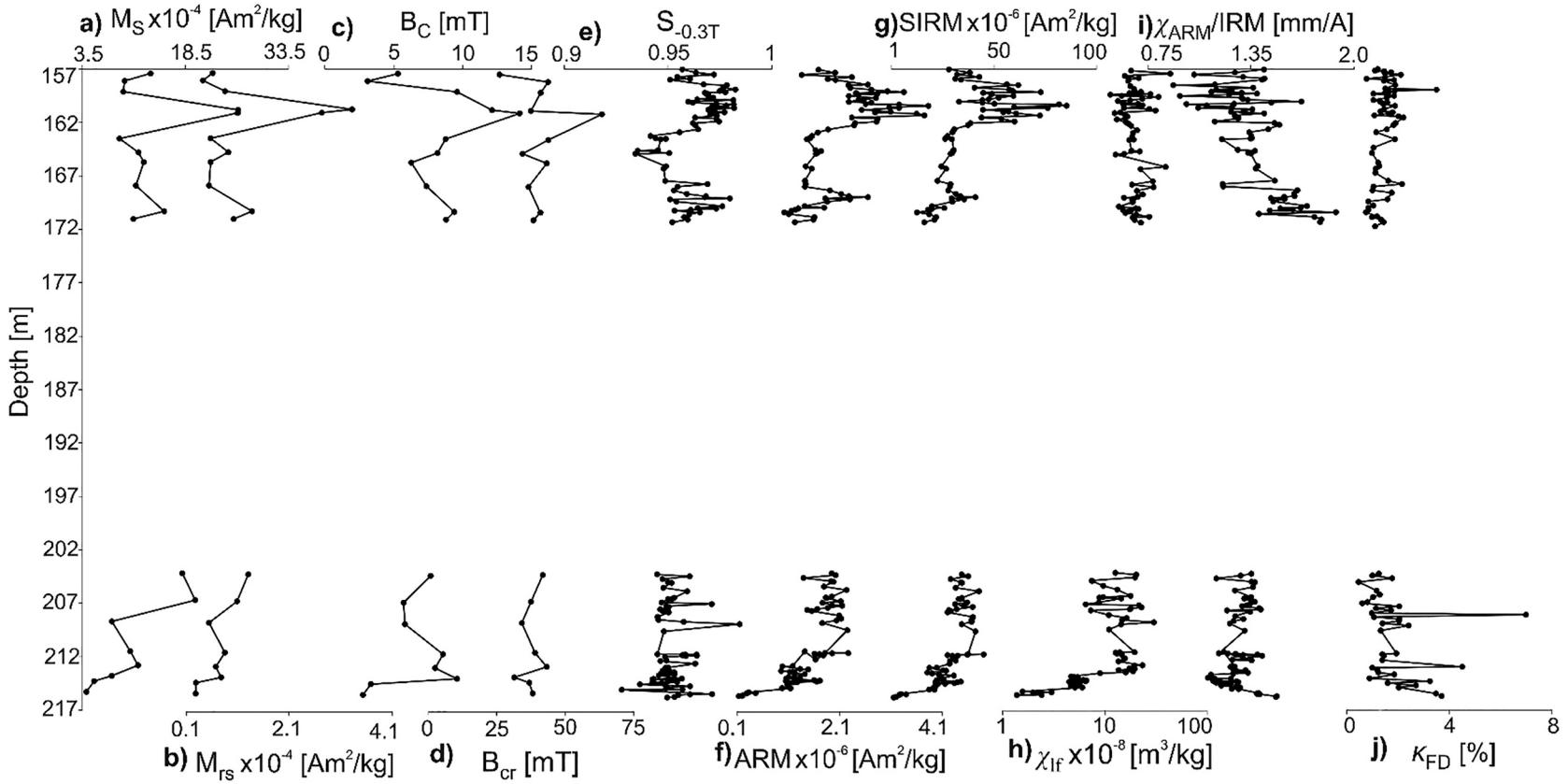

Fig. 4. Rock magnetic parameters of the investigated profile in depth intervals 157–172 m and 204–216 m.

4.3. FORC

The hysteresis loop of HB161–15 is dominated by a paramagnetic contribution (Fig. 5a), with M_{max} measured in ±220 mT being ~200 times larger than M_s. After removing the paramagnetic contribution, FORC measurements reveal a typical SD signature (Fig. 5b) with hysteresis parameters listed in Table 1. The FORC diagram resembles those obtained for magnetofossil-rich sediments, with a pronounced central ridge surrounded by oval contours, and a negative region in the lower-left part of the diagram (Fig. 5c). This signature has been described in Amor et al. (2022) as the result of a mixture of single- and multistranded fossil magnetosome chains. Both types of chains contribute to the central ridge, while transition between flux-closure and SD-like magnetic states in multistranded chains produce additional contributions above and below the central ridge. In magnetofossil-rich sediments, the ratio M_{cr}/M_{rs} between the central ridge magnetization M_{cr} and the saturation remanence M_{rs} amounts to 0.37–0.65% of M_{rs} (Amor et al., 2022). In HB161–15, M_{cr}/M_{rs} is close to the lower limit (Table 1), which means that FORC contributions above and below the central ridge are larger than the typical magnetofossil average. These contributions, which correspond to hysterons with a horizontal offset produced by internal fields in the Preisach-Néel model of the FORC function (Egli, 2021), are expected to lower χ_{ARM}/IRM below the range expected for non-interacting SD particles (e.g., magnetofossils) associated with the central ridge. Indeed, χ_{ARM}/IRM ≈ 1.35 mm/A for this sample is about half of the value expected for magnetofossils (Egli, 2004a). On the other hand, FORC signatures typical of non-SD detrital minerals, in the form of triangular contour lines diverging towards zero coercivity ($B_c = 0$) (Roberts et al., 2017; Egli, 2021) are absent. Along with $M_{rs}/M_s \approx 0.4$, these properties confirm the SD nature of the low-coercivity minerals contributing to the ferrimagnetic signature. This signature is retained throughout the sediment profile, despite a ~1 order of magnitude decrease of the SIRM below ~162 m, which means that the magnetic contribution of detrital minerals is either negligible, or it varies proportionally to the authigenic component, which, in the case of greigite-bearing sediment, can only originate from the reductive dissolution of

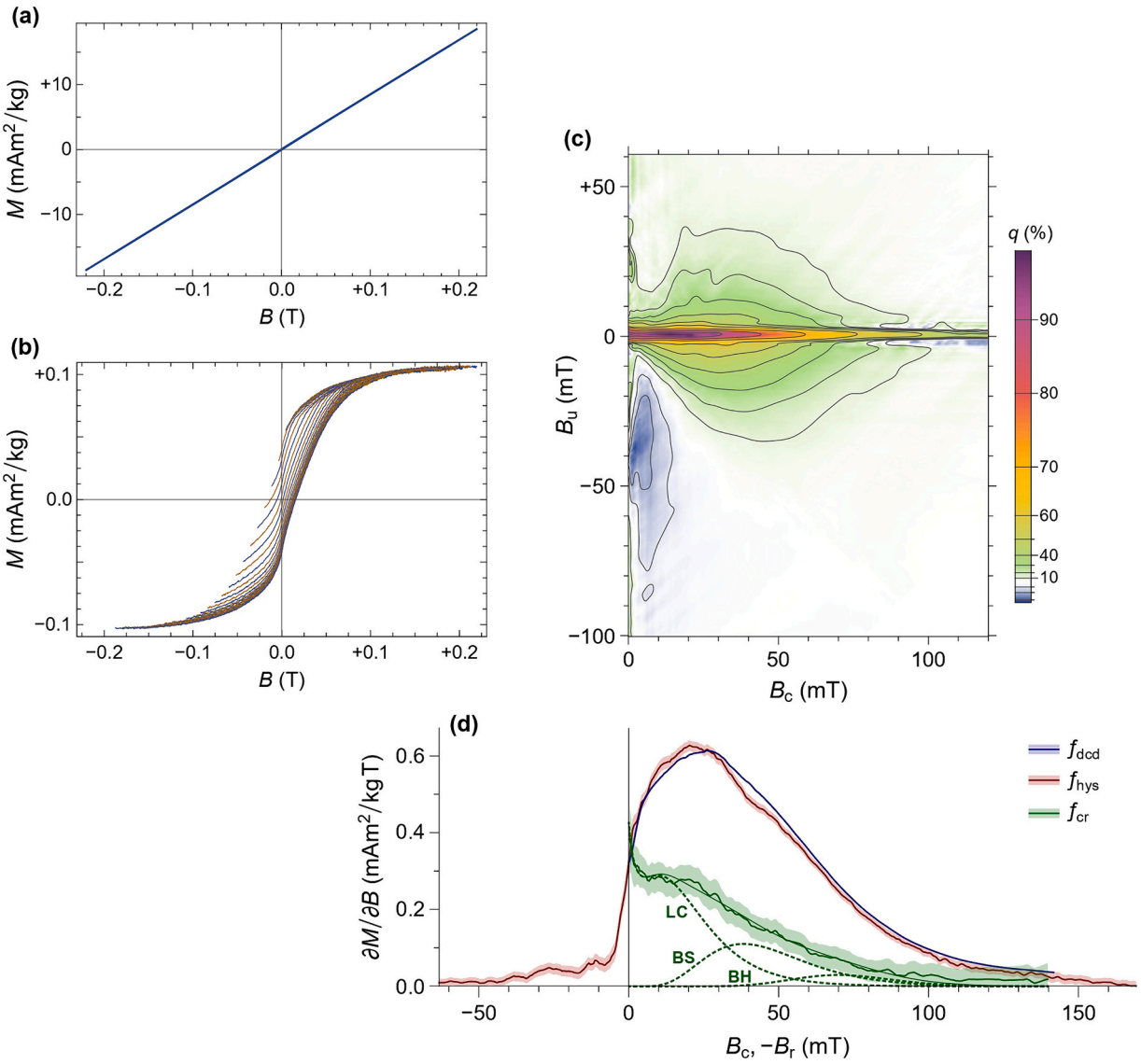

Fig. 5. (a) Stacked FORC measurements of sample HB161–15. (b) Same as (a) after subtracting the paramagnetic contribution $M = \chi_{hf} B$ with the high-field susceptibility (χ_{hf}) given in Table 1. One curve every 20 is shown for clarity (c) FORC diagram obtained from the corrected measurement stack in (b). Quantile contours (Egli, 2021) in 10% intervals show the total magnetization associated with FORC contributions outside the enclosed area. (d) Coercivity distribution obtained from FORC subsets corresponding to the DC demagnetization curve (f_{dcd}), the irreversible component of the lower hysteresis branch (f_{hys}), and the central ridge (f_{cr}), along with the three magnetic components LC, BS, and BH used to fit f_{cr}.

Table 1
Hysteresis and FORC properties of HB161–15 and HB162–38, compared to corresponding properties for the CBD-extractable fraction of a magnetofossil-rich sediment ("Mf-EM", from Ludwig et al., 2013), Pleistocene sediments containing greigite framboids ("UN080–22", from Scheidt et al., 2017), two greigite-bearing horizons in Holocene sediments ("α" and "β", from Ohneiser et al., 2024), and the corresponding central-ridge-free endmember representing authigenic greigite ("AGr-EM"). M_{forc}: total FORC magnetization; M_{sdrev}: total magnetization.

Parameter	Mf-EM	HB161–15	HB162–38	UN080–22	α	β	AGr-EM
χ_{hf} (10^{-8} m^3/kg)	3.25	10.55	17.83	4.88	5.93	11.54	6.54
χ_{hf}/M_s (10^{-5} m/A)	0.44	99	451	0.78	1.55	0.94	0.72
M_s (mAm^2/kg)	7.373	0.107	0.0395	6.3	3.818	12.28	9.06
M_{rs} (mAm^2/kg)	3.293	0.0426	0.0167	2.391	1.968	4.962	3.304
M_{cr} (mAm^2/kg)	2.143	0.0154	n/a	0.0435	0.129	0.109	0
B_c (mT)	20.78	15.94	13.44	23.71	33.42	34.66	34.33
B_{cr} (mT)	32.93	38.26	37.1	63.56	62.51	62.52	58.27
B_{cr}/B_c	1.585	2.4	2.758	2.681	1.87	1.804	1.697
M_{rs}/M_s	0.447	0.4	0.421	0.379	0.498	0.404	0.365
M_{rs}/M_{forc}	0.992	0.98	n/a	0.864	0.88	0.9	0.895
M_{cr}/M_{rs}	0.653	0.36	n/a	0.018	0.068	0.022	0
M_{sdrev}/M_{forc}	0.134	0.143	n/a	0.191	0.175	0.161	0.237

magnetite. The presence of a well-defined Verwey transition (Fig. 3b) excludes this hypothesis, enabling us to conclude that the FORC signature of HB161–15, one of the samples with largest M_{rs}, is purely diagenetic. The apparent lack of a detrital contribution can be explained by the dilution effect of carbonate precipitation and the simultaneous conversion of non-magnetic forms of iron into magnetic ones through reductive diagenesis.

An important difference between HB161–15 and magnetofossil-rich sediments is related to the coercivity distribution of the central ridge (f_{cr}). In the case of magnetofossils, f_{cr} peaks at 25–50 mT starting from almost zero at $B_c = 0$. The absence of SD switching processes near $B_c = 0$ is due to the strong uniaxial anisotropy of magnetosome chains (Ludwig et al., 2013; Heslop et al., 2014; Amor et al., 2022). On the other hand, the main peak of f_{cr} in HB161–15 is located at $B_c = 0$, followed by a steep decrease over the 0–5 mT interval, a plateau extending to ~25 mT, and finally an exponential-like decrease up to ~110 mT (Fig. 5c). This shape of f_{cr} has been fitted with a linear combination of four component: a one-sided exponential function of the form exp.(B_c/B_0)/B_0, and three skewed generalized Gaussian (*SGG*) functions (Egli, 2003) with the average properties of the coercivity components 'extracellular magnetite' (EX), and 'biogenic soft' (BS) and 'biogenic hard' (BH) magnetofossils (Egli, 2004a). The noisy character of the central ridge did not enable to optimize the shape parameters of EX, BS, and BH; nevertheless, data are well fitted with the predefined parameters over the 0–110 mT interval (Fig. 5d, Table 2). The exponential function accounts mainly for the 0–5 mT decrease of f_{cr}. On a logarithmic field scale, it is well approximated by $SGG(\log_{10}(B), \log_{10}(B_0) - 0.157, \sigma, q, p)$ with $\sigma = 0.666$, $q = 0.495$, $p = 2.33$. On a linear field scale, the *SGG* approximation diverges for $B < 0.1B_0$, which means that the coercivity component represented by exp.(B_c/B_0)/B_0 is intrinsically different from the other components in being the only one that describes SD switching processes with zero coercivity. This component is responsible for the discontinuous slope increase of all FORC measurements at $B = 0$ (Fig. 5b). Detection of slope discontinuities in magnetization curves, including the one caused by the central ridge, requires high-resolution measurements with elevated signal-to-noise ratio and a limitation of the smoothing factor over the corresponding field ranges (Egli, 2021). These conditions are seldomly met by published data; therefore, we cannot assess whether this feature, which has not been reported before, is a common occurrence in sedimentary materials.

EX and exp.(B_c/B_0)/B_0 contribute to a low-coercivity component, LC, which accounts for ~60% of M_{cr}. The second most important contribution to the central ridge is that of component BS (~31.5%), followed by BH (~8%). Components BS and BH are usually associated with equidimensional and elongated magnetofossils, respectively (Egli, 2004a; Amor et al., 2022). According to the above analysis, HB161–15 appears to be a mixture of three types of SD particles: two types of conventional magnetofossils contributing to the central ridge and oval contours around it, and the LC component, which appears mainly in the central ridge, as seen by the lack of vertical spread of the FORC function near $B_c = 0$. FORC signatures similar to component LC have been reported for sediments that experienced early stages of authigenic greigite formation (Rowan et al., 2009), where most greigite particles are SP at room temperature. The room temperature M_{rs} of these sediments is ~1 order of magnitude smaller than that of typical magnetofossil-bearing sediments, but still ~10 times larger than the magnetization of the LC component in HB161–15 (Table 1). The FORC diagrams of the greigite formation zone shown by Rowan et al. (2009) are dominated by a central ridge peaking at or very close to $B_c = 0$, and a vertical ridge along $B_c = 0$ in the lower half of the FORC space. This ridge is a characteristic signature of viscous SD particles (Pike et al., 2001): its amplitude is proportional to the relative proportion of particles with unblocking times comparable with the time required to acquire the first few points in each magnetization curve (Egli, 2021). A prominent vertical ridge is thus associated with grain size distributions peaking at or near the lower SD stability threshold (~25 nm for magnetite and greigite), as seen for instance in the case of pedogenic magnetite (Egli, 2021). The almost complete lack of a vertical ridge in HB161–15, along with M_{rs}/M_s values close to the expected value for stable SD particles, indicate that the LC component is associated with magnetic particles with a size distribution almost completely comprised within the SD stability range, that is, ~25–60 nm for equidimensional magnetite particles (Muxworthy and

Table 2
Parameters of the magnetic components used to fit the central ridge coercivity distribution. Numbers in italics refer to fixed values coinciding with the average of parameters reported in Egli (2004a).

Parameter	exp(B_c/B_0)/B_0	EX	BS	BH
M/M_{cr}, HB161–15	0.098	0.506	0.315	0.082
M/M_{cr}, magnetofossils	0.00596	0.29	0.587	0.117
B_0 (mT), HB161–15	3.44	–	–	–
μ	–	*1.261*	*1.643*	*1.856*
σ	–	*0.346*	*0.187*	*0.107*
q	–	*0.607*	*0.739*	*0.703*
p	–	*2.04*	*2*	*2*

Williams, 2009) and ~ 25–80 nm for equidimensional greigite particles (Muxworthy et al., 2013). This tight size constraint appears to be barely compatible with the usually broad size distribution of inorganically precipitated nano-magnetite crystals (e.g., Faivre et al., 2004), but the possibility of special formation pathways leading to tightly controlled sizes exist (Arató et al., 2005).

SD greigite with a narrow size distribution and FORC properties similar to those of the LC component, especially after oxidation in air, has been produced from a lepidocrocite precursor (Roud et al., 2022). In this example, hysteresis parameters follow a SP-SD mixing line on the Day plot, but FORC diagrams measured at room temperature lack a central ridge, similarly to the case of HB161–15. SP-SD mixing trends in the Day plot are characterized mainly by an increase of B_{cr}/B_c above the typical value of ~1.2 reported for fully blocked SD magnetite particles (Dunlop, 2002). However, the exact value of B_{cr}/B_c for blocked SD particles depends on the width of their coercivity distribution. Distributions containing significant near-zero coercivity contributions such as the LC distribution, yield B_{cr}/B_c values of ~2 or larger. This is because the hysteresis of particles with small B_{cr} resembles that of SP particles even when their magnetization is fully blocked. A non-viscous magnetic component with the characteristics of LC has never been reported before. Limited or absent magnetostatic interactions, which is evident for the 0–10 mT range of B_c, implies that LC particles in this coercivity range are well dispersed in the sediment matrix, with reciprocal distances several times larger than their size. This excludes the clustered SD greigite particles of Fig. 2 as possible candidates for the LC component, since the combination of magnetic interactions and magnetic viscosity leads invariably to FORC contributions with a diverging vertical spread near $B_c = 0$, as seen in spin glasses (Katzgraber et al., 2007).

We are therefore left with the problem of identifying the magnetic signature of SD greigite clusters detected with electron microscopy in the FORC diagram, keeping in mind that the images of Fig. 2 do not provide any information about the relative contribution of these clusters to the total remanent magnetization. Sediments with dominant authigenic SD greigite content are characterized by FORC signatures with a central maximum at B_c = 40–60 mT and $B_u \approx -5$ mT, surrounded by oval contour lines, and sometimes superimposed with faint traces of a central ridge (Rowan and Roberts, 2006; Vasiliev et al., 2007; Chang et al., 2009; Egli et al., 2010; Roberts et al., 2011). The central ridge turns out to be unrelated to authigenic greigite, as discussed later. The authigenic greigite endmember signature (Ohneiser et al., 2024) is clearly distinct from that of non-central ridge FORC contributions from magnetofossils (Fig. 6a, c), albeit the oval contours are typical for interacting SD particles in both cases. A distinctive feature of magnetite magnetofossils is the abrupt termination of the contours at the high-coercivity end of the upper quadrant (UT in Fig. 6a), which is also observed in micromagnetic simulations of multistranded magnetosome chains (Amor et al., 2022). Oval FORC contours in the authigenic greigite endmember are slightly stretched along the dashed diagonals depicted in Fig. 6c (feature MFI). This feature, along with the negative vertical offset of the central maximum, is reminiscent of the diagonal ridges caused by positive mean field interactions (e.g., Fig. 31 in Egli, 2021), overlapped with the classical Preisach signature of SD magnetic particles with strong magnetostatic interactions (Carvallo et al., 2005). These features are compatible with dense clusters of touching particles, such are greigite framboids. The authigenic greigite endmember also contains a vertical ridge along $B_c = 0$ (VS in Fig. 6c), which extends mainly over the lower quadrant. In the case of non-interacting, viscous SD particles, this ridge extends over the lower quadrant only (Lanci and Kent, 2018), because particles with initial positive saturation are not switched in $B_r = B_u > 0$. Extension of VS over the same positive range of B_u as the central peak can be explained by a positive bias of the switching field of viscous particles by local magnetostatic interactions.

The FORC signature of HB161–15 appears to be very close to that of the magnetofossil endmember (Fig. 6a). Nevertheless, there are hints pointing to a contribution from the authigenic greigite endmember, which include lack of the UT feature, and the added contribution from MFI and VS (arrows in Fig. 6b). Principal component analysis of FORC diagrams (FORC-PCA) could be used to infer the relative contribution of the magnetofossil and authigenic greigite endmember; however, the ferrimagnetic contribution is too weak to perform the required measurements on several samples (Section 3.3). Here, we avoid these limitations of FORC-PCA by using the existing FORC signatures of magnetofossil and authigenic greigite in Fig. 6a,c as endmembers contributing to HB161–15. This sample is expected to contain the following magnetic components: (1) magnetite magnetofossils, (2) greigite magnetofossils, (3) authigenic greigite. Greigite magnetofossils are expected to have similar properties as magnetite ones, with a central ridge contribution (Chen et al., 2014; Bai et al., 2022). This contribution is visible in all FORC measurements of greigite-bearing sediments in case of sufficient measurement quality. Magnetofossils can have variable proportions of central ridge and non-central ridge contributions,

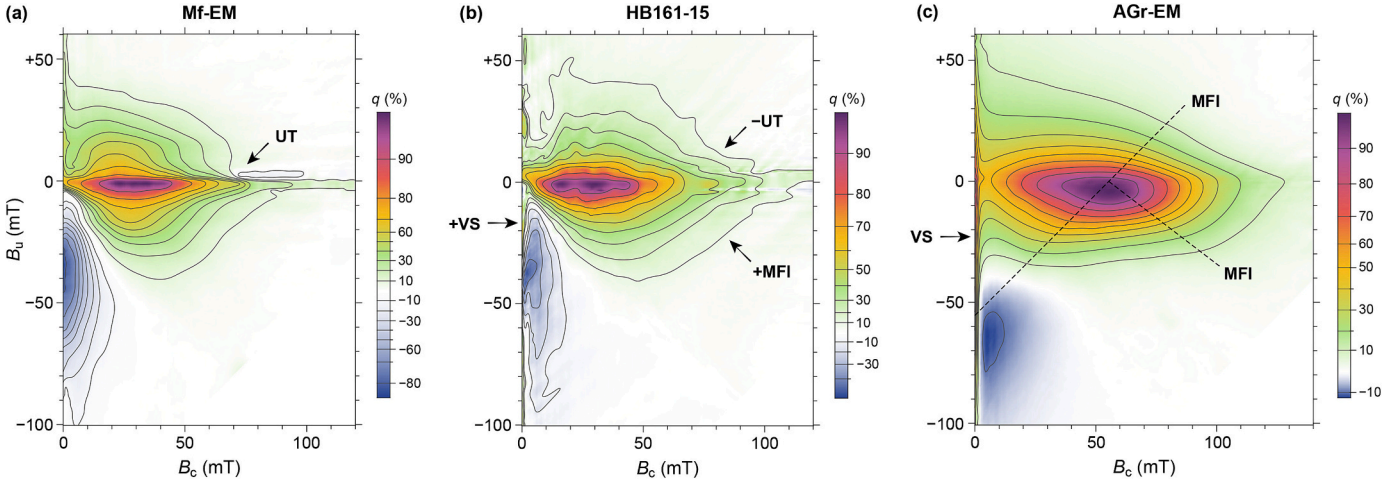

Fig. 6. Comparison between the FORC signatures of magnetofossils (a), sample HB161–15 (b), and authigenic greigite (c), after removing the central ridge when present. (a) was obtained from the difference between identical measurements of a magnetofossil-rich carbonate sediment, performed before and after chemical dissolution of the fine (mainly SD) magnetite fraction (data from Ludwig et al., 2013). "UT" is the abrupt termination of contours at the high-coercivity end of the upper quadrant, as predicted by Amor et al. (2022). (c) is the central-ridge-free FORC endmember obtained from two greigite-bearing lake sediment samples (Ohneiser et al., 2024). The dashed lines labelled with "MFI" highlight deviations from perfectly oval contours by the signature of positive mean field interactions. Quantile contours as in Fig. 5. Arrows in (b) indicate deviant features of HB161–15 with respect to (a), caused by the presence of authigenic greigite.

depending on the relative abundance of multistranded and fold-collapsed magnetosome chains (Amor et al., 2022). This additional degree of freedom in the magnetofossil signature can be eliminated by considering FORC diagrams where the central ridge has been removed with the procedure described in Egli (2013, 2021), as shown in Fig. 6. In this case, we assume that the central-ridge-free FORC function ρ of HB161–15 is a linear combination $a_{mf}\,\rho_{mf} + a_{agr}\,\rho_{agr}$ of the magnetofossil and authigenic greigite endmembers and calculate the corresponding coefficients a_{mf} and a_{agr} by linear regression. The solution $a_{mf} = 0.0120$ and $a_{agr} = 0.00398$ provides a reconstruction of ρ with a mean root square error of only ~2%. Accordingly, the authigenic greigite component accounts for ~31% of the total saturation remanence of HB161–15.

4.4. Paleomagnetism

4.4.1. NRM and ChRM

NRM values range between 1.5 and 85 $\times$ 10^{-8} Am^2/kg (Fig. 8c). These for sediments quite low values express a generally low concentration of ferromagnetic minerals. AF demagnetization to 50 mT removed, on average, 70% of NRM (Fig. 7). Secondary viscous remanent magnetization components were removed by 10 mT AF (e.g., Fig. 7b and d). Some samples acquired a gyroremanent magnetization (GRM) (see section 4.4.2). The median destructive field values (MDF) range between 5 and 85 mT (Fig. 8d). Demagnetization data for all samples are shown in Supplementary Table S1 (accepted samples) and S2 (rejected samples).

All ChRM directions were determined generally between AF steps of 20–40 mT (Fig. 7). Since the sediment cores are not azimuthally oriented, declination data is not interpretable. To evaluate the quality of the paleomagnetic data we use five selection criteria based on established procedures: i) maximum angular deviation (MAD) ≤15° (Kirschvink, 1980; Pick and Tauxe, 1993), ii) ChRM inclination ≥expected geocentric axial dipole (GAD) inclination at the site 67.6° − 45° cut off (McElhinny et al., 1996), iii) same magnetic polarity in neighboring samples except magnetic polarity transition zones, iv) NRM intensity difference of neighboring samples smaller than an order of magnitude, and v) k_3 inclination ≥75° (Hrouda and Kahan, 1991; Snowball et al., 2019). Samples that did not pass any of these criteria and yielded a scattered demagnetization behavior were excluded from further measurements and interpretation. ChRM inclination values from accepted samples (Fig. 8a) indicate two intervals with normal polarity between 163.2 and 165.5 m depth and 211.9–216 m depth, and reversed polarity in the remaining part of the core (see section 5.4 for discussion on polarity zones). The clear identification of different polarity intervals is considered to demonstrate the correct choice of quality criteria. MAD values of the accepted data are comprised between 2.1° and 14.9° (Fig. 8b). Kirschvink (1980) recommended samples with MAD ≤15° to be considered paleomagnetically reliable. McElhinny and McFadden (1999) considered samples with MAD <10° to be of good quality, while MAD <5° has been suggested for high-quality data (Johnson et al., 1998). In total, 48% and 10% of the accepted samples are characterized by MAD <10° and MAD <5°, respectively.

4.4.2. GRM acquisition during AF demagnetization

The acquisition of GRM in AF fields >40 mT was discovered during static AF demagnetization of NRM (e.g., Figs. 7a, c and d). In a large number of studies, this observation is interpreted as an evidence for the presence of greigite (e.g., Snowball and Thompson, 1990; Snowball,

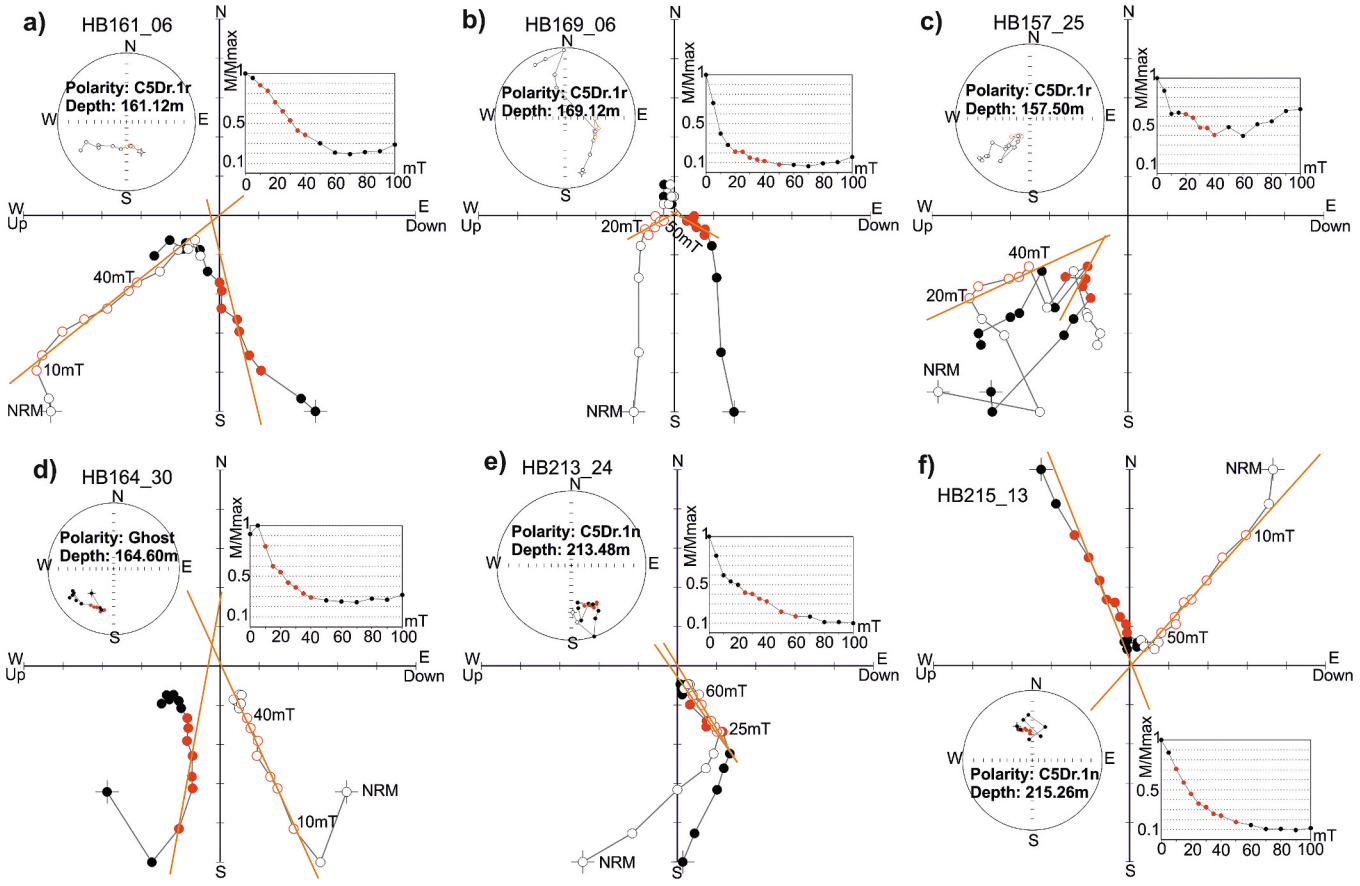

Fig. 7. (a-f) AF demagnetization curves, Zijderveld diagrams, and stereographic projections of representative samples. Red data points with AF demagnetization level (in mT) indicate the coercivity spectrum chosen to determine ChRM directions. Orange lines in Zijderveld diagrams show the principal component. Full (empty) circles represent horizontal (vertical) components in Zijderveld diagrams and normal (reversed) polarity in stereographic projections.

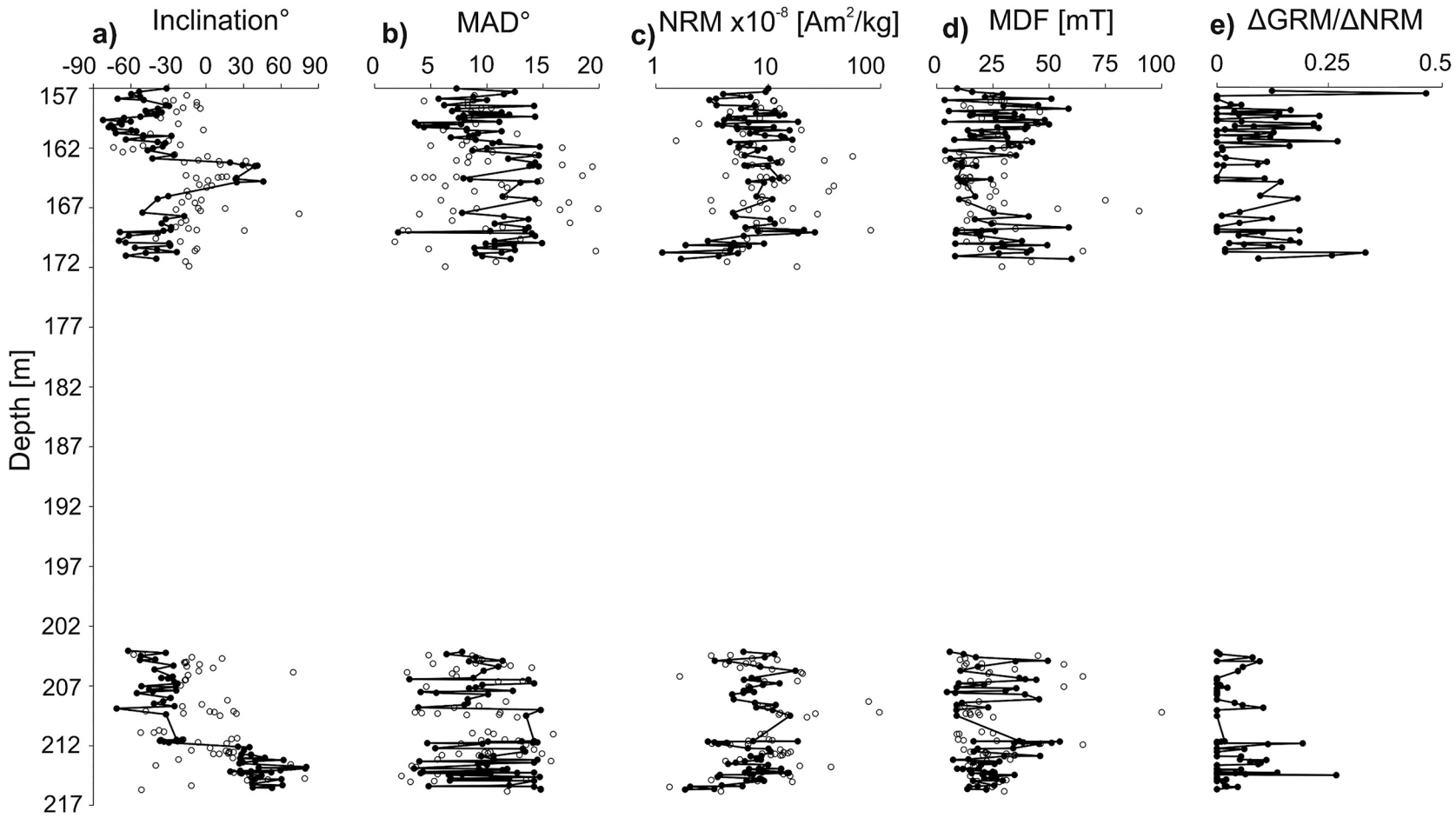

Fig. 8. Summary of paleomagnetic results. Full (empty) circles represent accepted (rejected) samples for (a) inclination, (b) MAD, (c) NRM, (d) MDF, and (e) ΔGRM/ΔNRM.

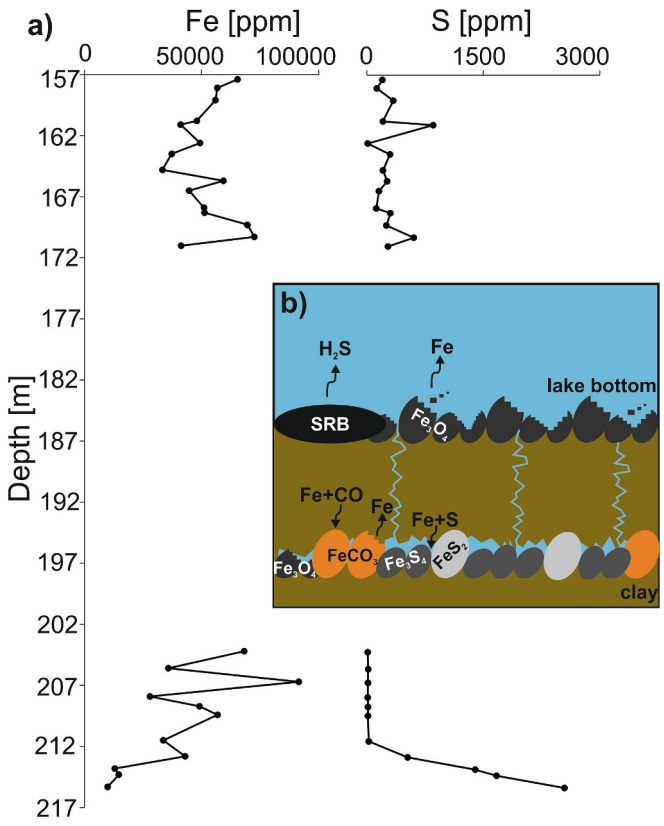

Fig. 9. (a) Changes in Fe and S content in XRF data. The average value for each one-meter sediment core section was used for the elemental compositions (Fe and S) due to fluctuations. (b) Representative sketch for iron sulfide formation in the Most Basin sediment (~157–212 m depth) with greigite dominance.

1997a, 1997b; Hu et al., 1998; Fu et al., 2008; Roberts et al., 2011; Duan et al., 2017, 2020; Caricchi et al., 2019; Just et al., 2019; Maffione and Herrero-Bervera, 2022). Although fine (titano)magnetite particles can also carry a GRM, the presence of greigite appears to be essential for the acquisition of a GRM in sediments (Duan et al., 2020). GRM is acquired by magnetic particles possessing multiple SD magnetic states that are sub-parallel to the main anisotropy axis (Potter and Stephenson, 2005). In greigite-bearing sediments, GRM is acquired mainly above B_{cr} (Stephenson, 1993; Hu et al., 1998). The acquired GRM vector is perpendicular to the last demagnetized axis (Snowball, 1997a; Sagnotti and Winkler, 1999), which is y-axis in our case (Supplementary Fig. S4). Consequently, the magnetization vector resulting from the superposition of a GRM to the remaining NRM deflects away from the origin or passes parallel to it (Finn et al., 2021).

GRM can be quantified using the ΔGRM/ΔNRM ratio of Fu et al. (2008). This ratio normalizes the difference between final value (FV) and minimum value (MV) of the magnetization with the difference between the initial value (IV) and MV. The ΔGRM/ΔNRM values are highly variable and generally comprised between 0 and 0.25 (Fig. 8e), compared to 0.2–0.8 for greigite-bearing horizons in Fu et al. (2008). Lower ΔGRM/ΔNRM values in our samples can be explained by a mixed magnetite/greigite composition, as discussed in Section 4.3, where greigite is the main GRM contributor.

Remarkably, our samples show no GRM during AF demagnetization of ARM and IRM. While the absence of GRM during IRM demagnetization might be explained by masking by the ~10^3 times larger IRM (Duan et al., 2020), the lack of GRM acquisition in AF demagnetization of ARM curves is somewhat unexpected. A possible explanation might be that the relative contribution of greigite to the NRM, which can be seen as a CRM, is larger than that of the ARM. In this case, the central ridge, which is the part of the FORC diagram contributing to large χ_{ARM}/IRM values, must be associated mainly with SD magnetite. The dominant contribution of greigite to the NRM is indirectly supported by the opposed trends of NRM intensity and χ_{ARM}/IRM over the 167–172 m interval: if large χ_{ARM}/IRM values are associated with magnetite contributions to the central ridge, the relative contribution of greigite decreases with depth, producing a decrease in NRM intensity if the NRM acquisition efficiency of greigite is larger than that of magnetite. This difference in NRM acquisition intensity can be expected if greigite acquired a CRM, whose intensity is comparable to that of an ARM (Pick and Tauxe, 1991), and magnetite a DRM, which is much smaller than an ARM (e.g., Ouyang et al., 2014).

5. Discussion

5.1. Magnetic mineralogy

The analyses presented in section 4 reveal a low concentration of magnetic minerals in the sediments. $\chi(T)$ measurements, provide evidence for sulfides and for a small fraction of magnetite. SEM/EDS analyses show closely packed greigite and pyrite aggregates indicating their diagenetic origin in a reducing sedimentary environment (Snowball, 1997a; Weaver et al., 2002; Rowan and Roberts, 2006; Larrasoaña et al., 2007; Vasiliev et al., 2007; Rowan et al., 2009; Roberts et al., 2011; Fu et al., 2015; Scheidt et al., 2017; Li et al., 2019; Ebert et al., 2020; Ahn et al., 2021; Liu et al., 2021). In addition, the acquisition of GRM during AF demagnetization of NRM of bulk sediment samples points towards the presence of greigite. Finer greigite and magnetite crystals also contribute significantly to the magnetic signature of samples. The lack of FORC signatures typical of larger particles indicates the magnetic properties to be dominated by SD minerals. Three magnetic components occur as isolated particles or chain of particles in the sediment matrix and contribute to the central ridge: in order of decreasing coercivity these are elongated magnetofossils (BH), equidimensional magnetofossils (BS), and unidentified non-viscous low-coercivity particles (LC) with small or vanishing single-particle anisotropy. The LC component is distinct from authigenic irregular-shaped magnetite particles with broad

Table 3
List of relevant quantities deduced from elemental and magnetic data.

Quantity	Value	Assumptions
χ_{hf} in HB161–15	10.55×10^{-8} m^3/kg	(measured)
χ_{hf} from total [S] assuming 100% pyrite composition	0.004×10^{-8} m^3/kg	$\chi_{hf} = 7.2 \times 10^{-8}$ m^3/kg for pure pyrite (Dahlin and Rule, 1993) and [S] = 240 ppm (Fig. 9a) entirely from pyrite
χ_{hf} from total [Fe] assuming 100% siderite composition	12×10^{-8} m^3/kg	$\chi_{hf} = 126 \times 10^{-8}$ m^3/kg for pure siderite (Jacobs, 1963) and [Fe] = 45,000 ppm (Fig. 9a) entirely from $FeCO_3$.
M_s in HB161–15	0.107 mAm^2/kg	(measured)
M_s from total [S] assuming 100% greigite composition	16 mAm^2/kg	$M_s \approx 31$ Am^2/kg for sedimentary greigite (Chang et al., 2008)
[S] from greigite in HB161–15	0.5 ppm or 40 μM (dry sediment)	Dry bulk density of sediment: 2.5 g/cm^3 (Dadey et al., 1992)
[Fe] from magnetite and greigite in HB161–15	1.2 ppm	$M_s = 92$ Am^2/kg for magnetite, 35% of the magnetization is carried by greigite

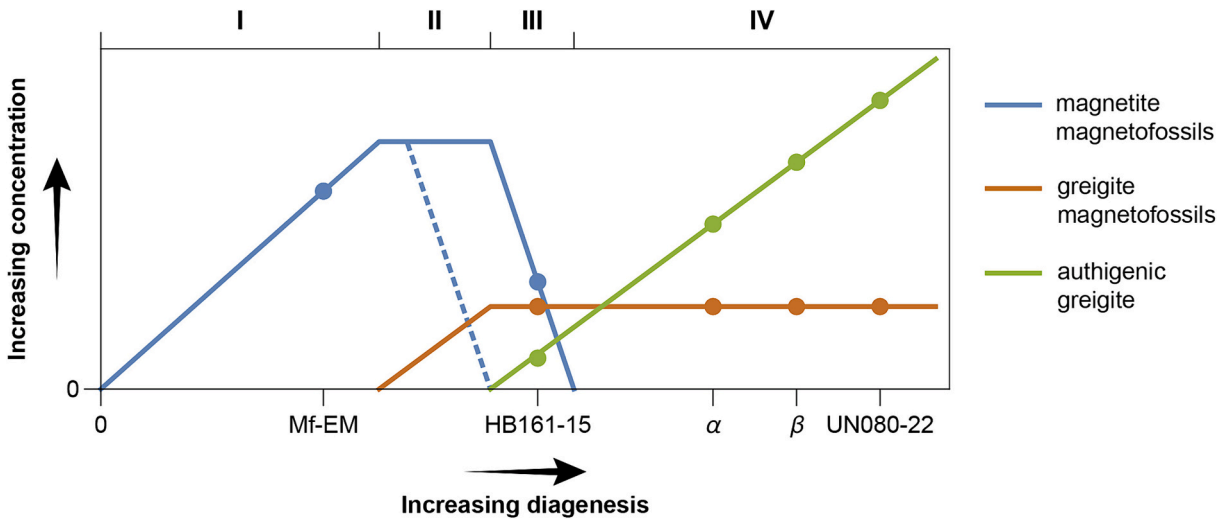

Fig. 10. Schematic representation of sequential magnetite and greigite formation in sediments with increasing degree of diagenesis. Dots represent the samples listed in Table 1 (not to scale).

size distributions encountered in soils (Geiss et al., 2008; Egli, 2021) and sediments (Gibbs-Eggar et al., 1999), which, unlike LC, are significantly viscous. Frequency dependencies of susceptibility mainly around 1.5–2.0% indicate a minor SP contribution in most samples; while the SP content deduced from the Day diagram (Fig. 3i) is largely overestimated, owing to the large B_{cr}/B_c values associated with component LC.

The FORC diagram of Fig. 5 bears the typical signature of magnetofossil-bearing sediments. The presence of authigenic greigite is not evident but hinted by a careful comparison with typical endmember signatures taken from the literature. The concentration of magnetic minerals is too weak to obtain specific endmembers from the sediment profile using FORC-PCA; however, the only available FORC diagram is precisely reproduced by a linear combination of magnetofossil (Ludwig et al., 2013) and authigenic greigite (Ohneiser et al., 2024) endmember signatures. Accordingly, the authigenic greigite contribution to M_{rs} is ~31%. Additional contributions from greigite magnetofossils are barely distinguishable from those of magnetite magnetofossils and cannot be quantified. The presence of a Verwey transition excludes the complete dissolution of magnetite. The mixed mineralogic composition of secondary magnetic minerals is also supported by (1) ARM data, with intermediate χ_{ARM}/IRM values being compatible with a mixture of magnetofossils and SD particles with magnetostatic interactions, such as framboidal greigite, (2) GRM data, with ΔGRM/ΔNRM values being lower than those reported for sediments composed solely from greigite, and (3) SEM/EDS analyses showing mixture of magnetite and fine greigite.

This analysis suggests that magnetite magnetofossils and authigenic greigite can coexist to a certain extent, despite the fact that greigite diagenesis is invariably accompanied by the dissolution of fine magnetite particles (Rowan and Roberts, 2006; Fu et al., 2008).

5.2. *A possible scenario for iron sulfide formation*

Authigenic greigite formation is associated with sulfate-reducing bacteria (SRB) under anaerobic conditions at the sediment-water interface and/or below the sediment surface (Berner, 1984; Hoffmann, 1992; Chang et al., 2008; Roberts et al., 2011). The end product of sulfate respiration is hydrogen sulfide (H_2S or HS^-; Sagnotti et al., 2005) which causes the dissolution of iron oxides (Berner, 1984). The dissolved Fe ions react with H_2S to produce paramagnetic pyrite as the end product of the reaction (Berner, 1984). Greigite is the intermediate product that forms as a precursor of pyrite (Roberts, 1995; O'Reilly et al., 2000; Liu et al., 2004; Chang et al., 2008, 2014; Roberts et al., 2011). Co-existence of magnetic iron oxides (magnetite magnetofossils) and diagenetic greigite in the Most Basin sediment core might indicate that magnetite dissolution was only partial (Fig. 9b). The partial magnetite preservation imposes an upper limit to the sulfide concentration [S^{2-}], which depends on the specific surface area A of the magnetite particles and a reaction rate k for pyrite-coated magnetite (Canfield and Berner, 1987; Canfield et al., 1992). Using the data in Egli (2004b), the maximum sulfide concentration must not exceed ~1 μM for partial magnetofossil preservation over tens of years. This is several orders of magnitude less than the total sulfur concentration in the analyzed sediment (~240 ppm or 20 mM, Fig. 9a), meaning that only a negligible fraction of the total sulfur concentration in sediment must have been available as dissolved S^{2-}. The lack of pore water H_2S might explain the preservation of magnetite. Interestingly, the upper limit for [S^{2-}] deduced from the estimated greigite content of sample HB161–15 (Table 3) comes closer to 1 μM, especially when considering that greigite did not precipitate instantaneously.

As far as Fe is concerned, only a vanishingly small fraction of it is associated with magnetic minerals (Table 3). This means that practically all Fe sits in paramagnetic minerals and contributes to the high-field susceptibility (χ_{hf}). Pyrite does not contribute significantly to χ_{hf} measured in sample HB161–15, due to the limited sulfur concentration and its small χ_{hf}. Typical χ_{hf} values of the order of 1×10^{-8} m^3/kg for clay minerals (Potter et al., 2019) are also insufficient to explain our measurements. On the other hand, siderite ($FeCO_3$) with an Fe concentration corresponding to the XRF measurements of Fig. 9a yields a result that matches the measured χ_{hf} in HB161–15 (Table 3). Siderite usually forms in environments with abundant dissolved iron and carbonate, but with small residual amounts of pore water H_2S (Sagnotti et al., 2005). The reduced iron from partially dissolved magnetite cannot react to form pyrite due to H_2S deficiency, accumulates in pore spaces, and reacts with carbonate to form siderite at depth (Sagnotti et al., 2005). In this case, iron sulfides were found to form after siderite (Fig. 9b). Since diagenetic mineral formation depends on the balance between reactive iron and sulfur (Berner, 1984; Roberts et al., 1996; Kao et al., 2004), the smaller amount of iron and increasing S content in the deepest part of the sedimentary section may have allowed the formation of larger pyrite crystals and smaller greigite framboids below 212 m depth. In contrast, the larger amount of reactive dissolved iron and the scarcity of sulfur between 157 m and 212 m depth, might have favored the precipitation of authigenic greigite over pyrite. The distribution of greigite in sediment must be patchy, because of the large random downcore variations of ΔGRM/ΔNRM (Fig. 8e). This is another property

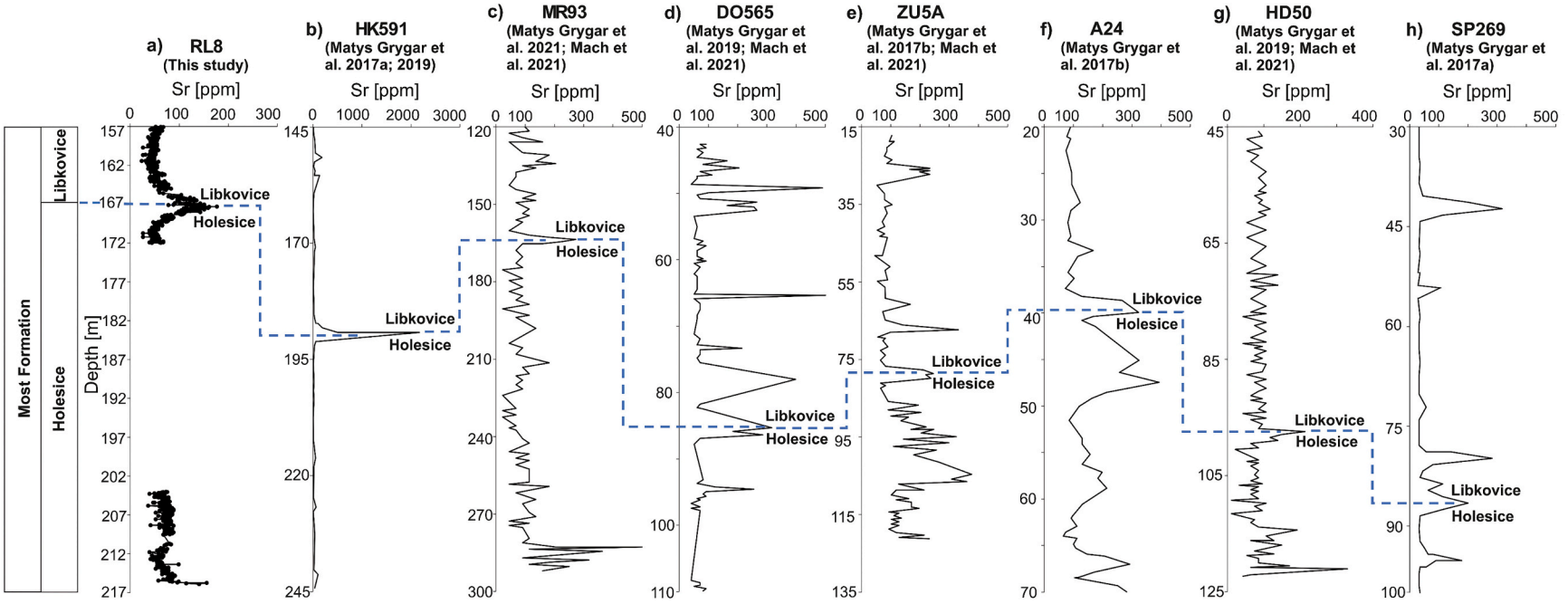

Fig. 11. Correlation of the sediment core from RL8 borehole (a) with the sediment cores from the boreholes in the previous studies (b-h) conducted in the Most Basin. The correlation of the drilling depths is based on the Sr anomaly (blue dashed lines) that occurs on the lithological boundary between the Holesice and Libkovice members of the Most Formation. (For interpretation of the references to color in this figure legend, the reader is referred to the web version of this article.)

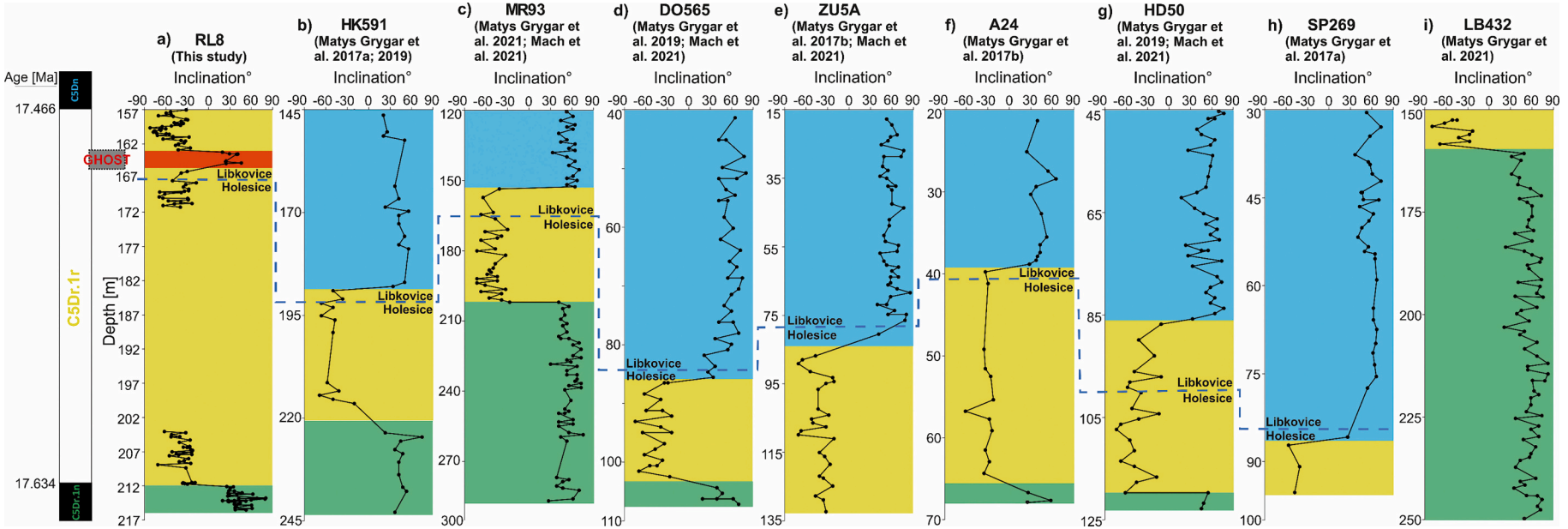

Fig. 12. Correlation of inclination data from this study (a) with the previous studies (b-i) conducted in the Most Basin. Green/yellow/blue/red backgrounds represent the C5Dr.1n/C5Dr.1r/C5Dn/Ghost magnetic polarities, respectively. Blue dashed lines represent the depth where is the Sr peak on the lithological boundary between the Holesice and Libkovice members used for the correlation of sediment cores in Fig. 11. Since XRF data for LB432 borehole is not available, magnetostratigraphic data for LB432 borehole is used for correlation. The ages in the magnetostratigraphic diagram (leftmost column) are according to GPTS 2020 (Kochhann et al., 2016; Ogg, 2020). (For interpretation of the references to color in this figure legend, the reader is referred to the web version of this article.)

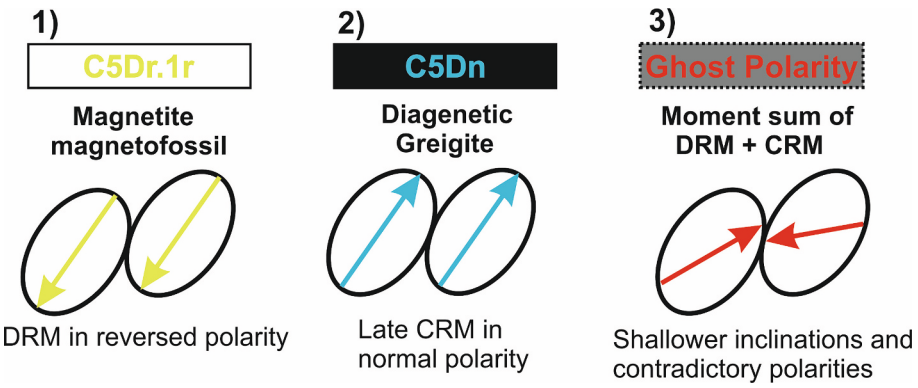

Fig. 13. Diagram describing the acquisition of a primary DRM and a late CRM at two different times causing a ghost polarity. See section 5.4 for a detailed explanation.

typical for the geochemical conditions described in Sagnotti et al. (2005).

5.3. Biogenic and authigenic greigite

Greigite-bearing sediments are usually characterized by the typical authigenic FORC signature of Fig. 6c. This signature is compatible with SD particles characterized by strong magnetostatic interactions and positive mean field interactions arising from magnetic exchange at contact points. These conditions are expected in framboidal greigite aggregates. Good-quality FORC measurements of greigite-bearing sediments often contain faint traces of a central ridge (e.g., Rowan and Roberts, 2006; Vasiliev et al., 2008; Ohneiser et al., 2024), which might be interpreted as the signature of greigite magnetosomes (Vasiliev et al., 2008), if one assumes that magnetite magnetosomes get completely dissolved during mature stages of reductive diagenesis. The M_{rs} contribution of this central ridge is of the order of 2–7% (Table 1), compared to >50% in the case of magnetofossil-bearing sediments. Interestingly, the absolute magnetization M_{cr} of the central ridge within the sediment profiles with highly variable authigenic greigite concentrations appear to be relatively constant, as shown by the example of lake sediment samples α and β in Table 1. The coexistence of magnetite magnetofossils and authigenic greigite discussed in section 5.2, and the presence of a relatively constant contribution of greigite magnetofossils in sediments characterized by increasing authigenic greigite contributions can be explained with the magnetite and greigite formation stage shown in Fig. 10.

Stage I is characterized by the formation of magnetite magnetofossils. The magnetofossil abundance depends on many factors, including the availability of assimilable Fe through the sedimentary iron cycle. This cycle is driven by organic matter, whose consumption creates a redox gradient. As sulphate reduction conditions are approached, magnetotactic bacteria species producing magnetite and greigite magnetosomes, or solely greigite magnetosomes, start to appear, leading to Stage II. Magnetite magnetosome production likely reaches a plateau at this stage. Direct precipitation of iron sulphides, including greigite, becomes possible at a later stage (Stage III), leading to the coexistence of biogenic and authigenic greigite. The presence of free HS^- and $S2^-$ ions start to dissolve fine-grained magnetite, including magnetite magnetofossils. As reductive diagenesis progresses, dissolution of fine-grained magnetite becomes complete, while greigite and other Fe sulphides continue to precipitate (Stage IV). Stage I samples are characterized by the typical magnetofossil signature in Fig. 6a. This signature is maintained during Stage II, because greigite magnetofossils are hardly distinguishable from magnetite ones. Furthermore, greigite magnetofossils appear to be much less abundant than magnetite ones, judging from the >1 order of magnitude lower central ridge magnetizations in greigite-bearing sediments (Table I). Sample HB161–15 is representative for Stage III, where magnetofossil and authigenic greigite signatures coexist. Depending on pH, dissolution of magnetite magnetofossils progresses more or less rapidly, and might be completed when authigenic greigite starts to precipitate (dashed line in Fig. 10). Sediments from Stage IV are dominated by the signature of authigenic greigite: since magnetite magnetofossils are completely dissolved, the presence of a minor central ridge contributions is due to the preservation of greigite magnetosomes produced during stages II and III. Accordingly, the relative contribution of the central ridge is inversely proportional to the amount of authigenic greigite produced during this stage. Samples UN080–22, α, and β with decreasing M_{cr}/M_{rs} values (Table 1) clearly represent this progression.

5.4. Ghost polarity as the evidence for timing of greigite formation

ChRM inclination values (Fig. 8a) reveal three magnetic polarity transition zones. The correlation of the core of the RL8 borehole to other cores of the Most Basin allows to link our paleomagnetic results to those of previous studies (Matys Grygar et al., 2017a, 2017b, 2019, 2021; Mach et al., 2021). Matys Grygar et al. (2017a) showed that Sr anomalies are easiest to use for the correlation between individual core profiles in the Most Basin. In particular, a sharp Sr anomaly just on the lithological boundary between the Holesice and Libkovice members is used to correlate the drilling depths of the sediment core from this study (Fig. 11a) with the other cores (Figs. 11b-h) in the basin. The correlated magnetostratigraphic data suggests that two of these magnetic polarity intervals belong to the C5Dr.1n normal polarity chron and C5Dr.1r reversed polarity chron (Fig. 12). In addition, another normal polarity interval occurs between 163.2 m and 165.5 m depth during the C5Dr.1r (Fig. 12a). The normal polarity interval does not correlate with the previous magnetostratigraphic data in the Most Basin (Figs. 12b-i) nor does it correspond to any magnetic polarity zone in GPTS 2020 (Ogg, 2020). The data from this normal polarity interval spans a time period of ~15 kyr (according to 13.5 cm/kyr sedimentation rate; Matys Grygar et al., 2017a, 2017b) eliminating the possibility of the occurrence of a magnetic excursion which is expected to show a faster (2–5 kyr) full reversal behavior (Ogg, 2020). Musgrave and Kars (2016) and Fu et al. (2015) reported 'ghost polarity zones' caused by a later authigenic greigite growth that produces intervals up to 5 m in length (depending

Table 4
Mean inclination values from each magnetic polarity zone calculated using the inclination-only method of McFadden and Reid (1982). *I*: inclination, *n*: number of samples, *k*: dispersion estimate, α_{95}: confidence ellipse.

Polarity	*n*	*I* (°)	*k*	α_{95} (°)
Ghost	8	24.1	1.9	59.5
C5Dr.1r	92	−43.9	12.2	4.3
C5Dr.1n	33	38.8	3.0	17.5

on sedimentation rate) that mimic an opposite polarity but up to 20 m below a real polarity transition. One possibility is that this may be due to a later diagenetic pore water migration event (Sagnotti et al., 2005) through the sediment column where abundant iron from siderite grains reacts with these fluids containing limited H_2S as discussed in section 5.2 (Fig. 9b). This mechanism possibly caused the formation of a diagenetic greigite considerably below the sulfate reduction zone. The timing of greigite formation may have created a complex mixture of a primary DRM (magnetite magnetofossils) with reversed polarity from the C5Dr.1r and a diagenetic CRM (greigite) with normal polarity from the following normal polarity zone (C5Dn, shown with blue color in Fig. 12). The combination of the two may result in 'transitional' directions (Liu et al., 2004; Rowan et al., 2009; Lucifora et al., 2012) in the magnetic moment sum of the grains that acquired a DRM and a CRM at two different times (Fig. 13). The resultant vector is highly variable from sample to sample, dependent on what proportions of primary magnetite and diagenetic greigite were present in a particular sample. Therefore, this smoothing effect of a late greigite growth may have caused a shallower mean inclination value of 24.1° (Table 4) for the ghost polarity interval that explains higher MAD values and higher rejection rate of the samples between 163 m and 166 m depth (Figs. 8a and b). Considering ~6 m sediment thickness (between 157 and 163.2 m depth) above the ghost polarity zone, diagenetic greigite may have formed at least ~45 kyr after magnetite magnetofossils (according to 13.5 cm/kyr sedimentation rate).

Additionally, the inclination values for the C5Dr.1n and C5Dr.1r fluctuate around mean values of +38.8° and −43.9°, respectively (Table 4). Considering that most of the samples are from polarity transition zones, the mean inclinations are expected to be lower than the GAD value. Furthermore, the inclination-only method of McFadden and Reid (1982) is expected to bias the mean to lower values than those calculated using Fisher (1953) statistics. However, the main reason for shallower mean inclinations is the smoothing effect of greigite discussed above. The steeper inclinations in some depth intervals may be related to local non-dipole field during the time of the mineral formation. Standing non-dipole field at mid-latitudes causes deviations from GAD value in a steeper direction especially in reversed polarities (Cox, 1975; Schneider and Kent, 1988).

6. Conclusions

Our results suggest that the NRM of the studied section in the Most Basin is carried by SD magnetite and authigenic greigite. Magnetic mineral characterization with FORC diagrams is particularly challenging, due to a strong paramagnetic background produced by siderite. High-precision FORC measurements of one sample revealed a pure SD signature with the following components: (1) magnetofossils with coercivity components similar to the BS and BH components previously found in magnetofossil-rich sediments, (2) a low-coercivity component with a signature similar to that of pedogenic magnetite, but with no magnetic viscosity and no magnetostatic interaction, which contains contributions from SD particles with virtually no magnetic anisotropy, which has never been observed before, and whose origin is unknown, and (3) authigenic greigite. Components (1) and (3) have overlapping FORC signatures and can be disentangled only with a quantitative analysis of the FORC diagram. Magnetite is likely associated with component (1), although greigite magnetofossils have been shown to have a compatible signature. Our measurements show that in case of samples containing magnetite and greigite, the fastest and easiest detection criterion for greigite is the GRM appearing in AF demagnetization curves of NRM. As revealed by the presence of component (2), caution should be used when interpreting SP + SD mixing lines in the Day plot, as the presence of magnetic components with vanishing coercivity tends to increase B_{cr}/B_c values regardless of the domain state.

Siderite usually forms in environments with abundant dissolved iron and carbonate, but with a lack of dissolved pore water H_2S. In this case, greigite is formed after siderite, with a patchy distribution that is reflected by the large random downcore variations of ΔGRM/ΔNRM.

The timing of remanence acquisition due to at least ~45 kyr late CRM recorded by diagenetic greigite creates a shift in the paleomagnetic data. This shift may cause magnetic polarity transition zones to appear in greater depths than the original depth, resulting in possible ghost polarities. The new magnetostratigraphic data provided detailed insight into the chronostratigraphy of the Most Formation. In addition, the new paleomagnetic record of the Early Miocene period from Central Europe is a significant contribution to the global geomagnetic data in terms of understanding the Earth's magnetic field behavior from iron sulfide-bearing sedimentary records acquiring a delayed CRM.

CRediT authorship contribution statement

Hakan Ucar: Writing – review & editing, Writing – original draft, Visualization, Validation, Project administration, Methodology, Investigation, Funding acquisition, Formal analysis, Data curation, Conceptualization. **Gunther Kletetschka:** Writing – review & editing, Validation, Supervision, Resources, Project administration, Methodology, Investigation, Funding acquisition, Formal analysis, Conceptualization. **Ramon Egli:** Writing – review & editing, Visualization, Validation, Software, Resources, Methodology, Investigation, Formal analysis, Data curation. **Karel Mach:** Writing – review & editing, Validation, Resources, Methodology, Investigation, Formal analysis, Conceptualization. **Michael S. Petronis:** Writing – review & editing, Validation, Resources, Methodology, Investigation, Formal analysis, Data curation. **Hana Grison:** Writing – review & editing, Validation, Resources, Methodology, Investigation, Formal analysis, Data curation. **Stephanie Scheidt:** Writing – review & editing, Validation, Methodology, Investigation, Formal analysis. **Petr Schnabl:** Writing – review & editing, Validation, Methodology, Investigation, Formal analysis. **Simon Kdyr:** Writing – review & editing, Validation, Methodology, Investigation, Formal analysis.

Declaration of competing interest

The authors declare that they have no known competing financial interests or personal relationships that could have appeared to influence the work reported in this paper.

Data availability

All data are incorporated into the article and its online supplementary material.

Acknowledgments

We thank all members of the Department of Paleomagnetism, Institute of Geology, Czech Academy of Sciences for allowing and helping us to measure the paleomagnetic samples, North Bohemian Mines, j.s.c. for providing the sediment cores, Radana Kavkova for helping with sediment core transportation, Radim Jedlicka, Viktor Golias, Jan Rohovec, and Noemi Meszarosova for helping with geochemical analyses, Greig Paterson for providing a modified version of the HystLab software, Jerome Gattacceca for valuable comments on the study, Dominique Jault for editorial handling of the manuscript, Mark J. Dekkers, and two anonymous reviewers for their insightful comments and suggestions which improved the manuscript. G.K. acknowledges the Czech Science Foundation (GACR); grant 23-06075S. M.S.P. acknowledges support from the National Science Foundation grant DMR-2122108 (PREM) and the Fulbright program, which funded his visiting fellowship at Charles University. The publication is in concordance with research plan of the Institute of Geology of the Czech Academy of Sciences (No. RVO67985831). The research was supported by the Charles University Grant Agency (project no. 265321).

This paper is dedicated to Dr. Miroslav Krs who pioneered the research on greigite and passed away on May 21, 2023 at the age of 95 years.

Appendix A. Supplementary data

Supplementary data to this article can be found online at https://doi.org/10.1016/j.pepi.2024.107216.

References

Ahn, H., Lim, J., Kim, S.W., 2021. Magnetic properties of a Holocene sediment Core from the Yeongsan estuary, Southwest Korea: implications for diagenetic effects and availability as Paleoenvironmental proxies. Front. Earth Sci. 9, 593332 https://doi.org/10.3389/feart.2021.593332.

Amor, M., Wan, J., Egli, R., Carlut, J., Gatel, C., Andersen, I.M., Snoeck, E., Komeili, A., 2022. Key signatures of magnetofossils elucidated by mutant magnetotactic bacteria and micromagnetic calculations. J. Geophys. Res. 127 https://doi.org/10.1029/2021JB023239 e2021JB023239.

Arató, B., Szányi, Z., Flies, C., Schüler, D., Frankel, R.B., Buseck, P.R., Pósfai, M., 2005. Crystal-size and shape distributions of magnetite from uncultured magnetotactic bacteria as a potential biomarker. Am. Mineral. 90, 1233–1241. https://doi.org/10.2138/am.2005.1778.

Babinszki, E., Márton, E., Márton, P., Ferenc Kiss, L., 2007. Widespread occurrence of greigite in the sediments of Lake Pannon: implications for environment and magnetostratigraphy. Palaeogeogr. Palaeoclimatol. Palaeoecol. 252, 626–636. https://doi.org/10.1016/j.palaeo.2007.06.001.

Bai, F., Chang, L., Pei, Z., Harrison, R.J., Winklhofer, M., 2022. Magnetic biosignatures of magnetosomal greigite from micromagnetic calculation. Geophys. Res. Lett. 49 (10) https://doi.org/10.1029/2022GL098437 e2022GL098437.

Berner, R.A., 1984. Sedimentary pyrite formation: An update. Geochim. Cosmochim. Acta 48, 605–615. https://doi.org/10.1016/0016-7037(84)90089-9.

Bloemendal, J., King, J.W., Hall, F.R., Doh, S.-J., 1992. Rock magnetism of late Neogene and Pleistocene deep-sea sediments: relationship to sediment source, diagenetic processes, and sediment lithology. J. Geophys. Res. Solid Earth 97, 4361–4375. https://doi.org/10.1029/91JB03068.

Canfield, D.E., Berner, R.A., 1987. Dissolution and pyritization of magnetite in anoxic marine sediments. Geochim. Cosmochim. Acta 51, 645–659. https://doi.org/10.1016/0016-7037(87)90076-7.

Canfield, D.E., Raiswell, R., Bottrell, S., 1992. The reactivity of sedimentary iron minerals toward sulphide. Am. J. Sci. 292, 659–683. https://doi.org/10.2475/ajs.292.9.659.

Caricchi, C., Lucchi, R.G., Sagnotti, L., Macrì, P., Di Roberto, A., Del Carlo, P., Husum, K., Laberg, J.S., Morigi, C., 2019. A high-resolution geomagnetic relative Paleointensity record from the Arctic Ocean deep-water gateway deposits during the last 60 kyr. Geochem. Geophys. Geosyst. 20, 2355–2377. https://doi.org/10.1029/2018GC007955.

Carvallo, C., Dunlop, D.J., Özdemir, Ö., 2005. Experimental comparison of FORC and remanent Preisach diagrams. Geophys. J. Int. 162, 747–754.

Chadima, M., Hrouda, F., 2006. Remasoft 3.0-a user friendly paleomagnetic data browser and analyzer. XXVII Travaux Geophysiques. 20–21.

Chang, L., Roberts, A.P., Tang, Y., Rainford, B.D., Muxworthy, A.R., Chen, Q., 2008. Fundamental magnetic parameters from pure synthetic greigite (Fe_3S_4). J. Geophys. Res. Solid Earth 113, B06104. https://doi.org/10.1029/2007JB005502.

Chang, L., Roberts, A.P., Rowan, C.J., Tang, Y., Pruner, P., Chen, Q., Horng, C.-S., 2009. Low-temperature magnetic properties of greigite (Fe_3S_4). Geochem. Geophys. Geosyst. 10 https://doi.org/10.1029/2008GC002276. Q01Y04.

Chang, L., Vasiliev, I., van Baak, C., Krijgsman, W., Dekkers, M.J., Roberts, A.P., Gerald, J.D.F., van Hoesel, A., Winklhofer, M., 2014. Identification and environmental interpretation of diagenetic and biogenic greigite in sediments: a lesson from the Messinian Black Sea. Geochem. Geophys. Geosyst. 15, 3612–3627. https://doi.org/10.1002/2014GC005411.

Chen, A.P., Berounsky, V.M., Chan, M.K., Blackford, M.G., Cady, C., Moskowitz, B.M., Kraal, P., Lima, E.A., Kopp, R.E., Lumpkin, G.R., Weiss, B.P., 2014. Magnetic properties of uncultivated magnetotactic bacteria and their contribution to a stratified estuary iron cycle. Nat. Commun. 5, 4797. https://doi.org/10.1038/ncomms5797.

Chen, Y., Zhang, W., Nian, X., Sun, Q., Ge, C., Hutchinson, S.M., Cheng, Q., Wang, F., Chen, J., Zhao, X., 2021. Greigite as an Indicator for salinity and sedimentation rate change: evidence from the Yangtze River Delta, China. J. Geophys. Res. Solid Earth 126. https://doi.org/10.1029/2020JB021085 e2020JB021085.

Cox, A., 1975. The frequency of geomagnetic reversals and the symmetry of the nondipole field. Rev. Geophys. 13, 35. https://doi.org/10.1029/RG013i003p00035.

Dadey, K.A., Janecek, T., Klaus, A., 1992. Dry-bulk density: its use and determination. In: Proceedings of the Ocean Drilling Program, Scientific Results, 126, pp. 551–554.

Dahlin, D.C., Rule, A.R., 1993. Magnetic Susceptibility of Minerals in High Magnetic Fields, Report of Investigations 9449. Bureau of Mines, United States Department of the Interior.

Day, R., Fuller, M., Schmidt, V.A., 1977. Hysteresis properties of titanomagnetites: grain-size and compositional dependence. Phys. Earth Planet. Inter. 13, 260–267. https://doi.org/10.1016/0031-9201(77)90108-X.

Dearing, J.A., Dann, R.J.L., Hay, K., Lees, J.A., Loveland, P.J., Maher, B.A., O'Grady, K., 1996. Frequency-dependent susceptibility measurements of environmental materials. Geophys. J. Int. 124, 228–240. https://doi.org/10.1111/j.1365-246X.1996.tb06366.x.

Dekkers, Mark J., Schoonen, M.A.A., 1996. Magnetic properties of hydrothermally synthesized greigite (Fe_3S_4)-I. Rock magnetic parameters at room temperature. Geophys. J. Int. 126, 360–368. https://doi.org/10.1111/j.1365-246X.1996.tb05296.x.

Dekkers, M.J., Passier, H.F., Schoonen, M.A.A., 2000. Magnetic properties of hydrothermally synthesized greigite (Fe_3S_4)-II. High- and low-temperature characteristics. Geophys. J. Int. 141, 809–819. https://doi.org/10.1046/j.1365-246x.2000.00129.x.

Demory, F., Nowaczyk, N.R., Witt, A., Oberhänsli, H., 2005. High-resolution magnetostratigraphy of late quaternary sediments from Lake Baikal, Siberia: timing of intracontinental paleoclimatic responses. Glob. Planet. Chang. 46 (1–4), 167–186. https://doi.org/10.1016/j.gloplacha.2004.09.016.

Duan, Z., Liu, Q., Gai, C., Zhao, X., 2017. Magnetostratigraphic and environmental implications of greigite (Fe_3S_4) formation from hole U1433A of the IODP expedition 349, South China Sea. Mar. Geol. 394, 82–97. https://doi.org/10.1016/j.margeo.2017.02.008.

Duan, Z., Liu, Q., Qin, H., Zhao, X., Gao, X., 2020. Behavior of Greigite-bearing marine sediments during AF and thermal demagnetization and its significance. Geochem. Geophys. Geosyst. 21 https://doi.org/10.1029/2019GC008635 e2019GC00863.

Dunlop, D.J., 2002. Theory and application of the Day plot (M_{rs}/M_s versus H_{cr}/H_c) 1. Theoretical curves and tests using titanomagnetite data. J. Geophys. Res. Solid Earth 107, 2056. https://doi.org/10.1029/2001JB000486.

Ebert, Y., Shaar, R., Levy, E.J., Zhao, X., Roberts, A.P., Stein, M., 2020. Magnetic properties of late Holocene Dead Sea sediments as a monitor of regional hydroclimate. Geochem. Geophys. Geosyst. 21 https://doi.org/10.1029/2020GC009176 e2020GC009176.

Egli, R., 2003. Analysis of the field dependence of remanent magnetization curves. J. Geophys. Res. 108, 2081. https://doi.org/10.1029/2002JB002023.

Egli, R., 2004a. Characterization of individual rock magnetic components using the analysis of remanence curves, 1. Unmixing natural sediments. Stud. Geophys. Geod. 48, 391–446. https://doi.org/10.1023/B:SGEG.0000020839.45304.6d.

Egli, R., 2004b. Characterization of individual rock magnetic components using the analysis of remanence curves, 3. Biogenic magnetite and natural processes in lakes. Phys. Chem. Earth 29, 869–884. https://doi.org/10.1016/j.pce.2004.03.010.

Egli, R., 2006. Theoretical considerations on the anhysteretic remanent magnetization of interacting particles with uniaxial anisotropy. J. Geophys. Res. Solid Earth 111. https://doi.org/10.1029/2006JB004577. B12S18.

Egli, R., 2013. VARIFORC: An optimized protocol for calculating non-regular first-order reversal curve (FORC) diagrams. Glob. Planet. Chang. 110, 302–320. https://doi.org/10.1016/j.gloplacha.2013.08.003.

Egli, R., 2021. Magnetic characterization of geologic materials with first-order reversal-curves. In: Franco, V., Dodrill, B. (Eds.), Magnetic Measurement Techniques for Materials Characterization. Springer Nature Publishing Group, pp. 455–604. https://doi.org/10.1063/978-3-030-70443-8_17.

Egli, R., Lowrie, W., 2002. Anhysteretic remanent magnetization of fine magnetic particles. J. Geophys. Res. Solid Earth 107, 2209. https://doi.org/10.1029/2001JB000671.

Egli, R., Chen, A.P., Winklhofer, M., Kodama, K.P., Horng, C.-S., 2010. Detection of non-interacting single domain particles using first-order reversal curve diagrams. Geochem. Geophys. Geosyst. 11 https://doi.org/10.1029/2009GC002916. Q01Z11.

Fabian, K., 2003. Some additional parameters to estimate domain state from isothermal magnetization measurements. Earth Planet. Sci. Lett. 213, 337–345. https://doi.org/10.1016/S0012-821X(03)00329-7.

Faivre, D., Agrinier, P., Menguy, N., Zuddas, P., Pachana, K., Gloter, A., Laval, J.-Y., Guyot, F., 2004. Mineralogical and isotopic properties of inorganic nanocrystalline magnetite. Geochim. Cosmochim. Acta 68, 4395–4403. https://doi.org/10.1016/j.gca.2004.03.016.

Fassbinder, J.W.E., Stanjek, H., 1994. Magnetic properties of biogenic soil greigite (Fe_3S_4). Geophys. Res. Lett. 21, 2349–2352. https://doi.org/10.1029/94GL02506.

Finn, D., Gilder, S., Coe, R., Pike, A., 2021. Effect of gyroremenance on relative paleointensity estimates applied to ignimbrite. Phys. Earth Planet. Inter. 318, 106769 https://doi.org/10.1016/j.pepi.2021.106769.

Fu, Y., von Dobeneck, T., Franke, C., Heslop, D., Kasten, S., 2008. Rock magnetic identification and geochemical process models of greigite formation in quaternary marine sediments from the Gulf of Mexico (IODP hole U1319A). Earth Planet. Sci. Lett. 275, 233–245. https://doi.org/10.1016/j.epsl.2008.07.034.

Fu, C., Bloemendal, J., Qiang, X., Hill, M.J., An, Z., 2015. Occurrence of greigite in the Pliocene sediments of Lake Qinghai, China, and its paleoenvironmental and paleomagnetic implications: Greigite in the Pliocene lake sediments. Geochem. Geophys. Geosyst. 16, 1293–1306. https://doi.org/10.1002/2014GC005677.

Geiss, C.E., Egli, R., Zanner, W., 2008. Direct estimates of pedogenic magnetite as a tool to reconstruct past climates from buried soils. J. Geophys. Res. 113, B11102. https://doi.org/10.1029/2008JB005669.

Gibbs-Eggar, Z., Jude, B., Dominik, J., Loizeau, J.-L., Oldfield, F., 1999. Possible evidence for dissimilatory bacterial magnetite dominating the magnetic properties of recent lake sediments. Earth Planet. Sci. Lett. 168, 1–6. https://doi.org/10.1016/S0012-821X(99)00054-0.

Heslop, D., Roberts, A.P., Chang, L., 2014. Characterizing magnetofossils from first-order reversal curve (FORC) central ridge signatures. Geochem. Geophys. Geosyst. 15, 2170–2179. https://doi.org/10.1002/2014CGC005291.

Hoffmann, V., 1992. Greigite (Fe_3S_4): magnetic properties and first domain observations. Phys. Earth Planet. Inter. 70, 288–301. https://doi.org/10.1016/0031-9201(92)90195-2.

Hrouda, F., 1982. Magnetic anisotropy of rocks and its application in geology and geophysics. Surv. Geophys. 5, 37–82. https://doi.org/10.1007/BF01450244.
Hrouda, F., Kahan, Š., 1991. The magnetic fabric relationship between sedimentary and basement nappes in the high Tatra Mountains, N. Slovakia. J. Struct. Geol. 13, 431–442. https://doi.org/10.1016/0191-8141(91)90016-C.
Hrouda, F., Pokorný, J., 2011. Extremely high demands for measurement accuracy in precise determination of frequency-dependent magnetic susceptibility of rocks and soils. Stud. Geophys. Geod. 55, 667–681. https://doi.org/10.1007/s11200-010-0079-6.
Hu, S., Appel, E., Hoffmann, V., Schmahl, W.W., Wang, S., 1998. Gyromagnetic remanence acquired by greigite (Fe_3S_4) during static three-axis alternating field demagnetization: GRM acquired by greigite. Geophys. J. Int. 134, 831–842. https://doi.org/10.1046/j.1365-246x.1998.00627.x.
Jacobs, I.S., 1963. Metamagnetism of siderite ($FeCO_3$). J. Appl. Phys. 34, 1106–1107. https://doi.org/10.1063/1.1729389.
Jelinek, V., 1981. Characterization of the magnetic fabric of rocks. Tectonophysics 79, T63–T67. https://doi.org/10.1016/0040-1951(81)90110-4.
Jiang, W.-T., Horng, C.-S., Roberts, A.P., Peacor, D.R., 2001. Contradictory magnetic polarities in sediments and variable timing of neoformation of authigenic greigite. Earth Planet. Sci. Lett. 193, 1–12. https://doi.org/10.1016/S0012-821X(01)00497-6.
Johnson, C.L., Wijbrans, J.R., Constable, C.G., Gee, J., Staudigel, H., Tauxe, L., Forjaz, V.-H., Salgueiro, M., 1998. $^{40}Ar/^{39}Ar$ ages and paleomagnetism of São Miguel lavas, Azores. Earth Planet. Sci. Lett. 160, 637–649. https://doi.org/10.1016/S0012-821X(98)00117-4.
Just, J., Sagnotti, L., Nowaczyk, N.R., Francke, A., Wagner, B., 2019. Recordings of fast Paleomagnetic reversals in a 1.2 ma Greigite-rich sediment archive from Lake Ohrid, Balkans. J. Geophys. Res. Solid Earth 124, 12445–12464. https://doi.org/10.1029/2019JB018297.
Kao, S.-J., Horng, C.-S., Roberts, A.P., Liu, K.-K., 2004. Carbon–sulfur–iron relationships in sedimentary rocks from southwestern Taiwan: influence of geochemical environment on greigite and pyrrhotite formation. Chem. Geol. 203, 153–168. https://doi.org/10.1016/j.chemgeo.2003.09.007.
Katzgraber, H.G., Hérisson, D., Östh, M., Nordblad, P., Ito, A., Katori, H.A., 2007. Finite versus zero-temperature hysteretic behavior of spin glasses: experiment and theory. Phys. Rev. B 76, 092408. https://doi.org/10.1103/PhysRevB.76.092408.
Kędzierski, M., Uchman, A., Sawlowicz, Z., Briguglio, A., 2015. Fossilized bioelectric wire – the trace fossil Trichichnus. Biogeosciences 12, 2301–2309. https://doi.org/10.5194/bg-12-2301-2015.
Kirschvink, J.L., 1980. The least-squares line and plane and the analysis of palaeomagnetic data. Geophys. J. Int. 62, 699–718. https://doi.org/10.1111/j.1365-246X.1980.tb02601.x.
Kochhann, K.G.D., Holbourn, A., Kuhnt, W., Channell, J.E.T., Lyle, M., Shackford, J.K., Wilkens, R.H., Andersen, N., 2016. Eccentricity pacing of eastern equatorial Pacific carbonate dissolution cycles during the Miocene climatic optimum. Paleoceanography 31, 1176–1192. https://doi.org/10.1002/2016PA002988.
Krs, M., Krsová, M., Pruner, P., Zeman, A., Novák, F., Jansa, J., 1990. A petromagnetic study of Miocene rocks bearing micro-organic material and the magnetic mineral greigite (Sokolov and Cheb basins, Czechoslovakia). Phys. Earth Planet. Inter. 63 (1–2), 98–112. https://doi.org/10.1016/0031-9201(90)90064-5.
Krs, M., Krsová, M., Pruner, P., Kouklíková, L., 1991. On the detailed magnetostratigraphy of greigite—(Smythite) mineralization, Sokolov Brown-Coal Basin, bohemia. Stud. Geophys. Geod. 35 (4), 267–284. https://doi.org/10.1007/BF01613973.
Krs, M., Novák, F., Krsová, M., Pruner, P., Kouklíková, L., Jansa, J., 1992. Magnetic properties and metastability of greigite-smythite mineralization in brown-coal basins of the Krušné hory Piedmont, Bohemia. Phys. Earth Planet. Inter. 70, 273–287. https://doi.org/10.1016/0031-9201(92)90194-Z.
Krs, M., Novák, F., Krsová, M., Pruner, P., Jansa, J., 1993. Magnetic properties, self-reversal remanence and thermal alteration products of smythite. Stud. Geophys. Geod. 37, 382–400. https://doi.org/10.1007/BF01613584.
Lanci, L., Kent, D.V., 2018. Forward modeling of thermally activated single-domain magnetic particles applied to first-order reversal curves. J. Geophys. Res. Solid Earth 123 (5), 3287–3300.
Larrasoaña, J.C., Roberts, A.P., Musgrave, R.J., Gràcia, E., Piñero, E., Vega, M., Martínez-Ruiz, F., 2007. Diagenetic formation of greigite and pyrrhotite in gas hydrate marine sedimentary systems. Earth Planet. Sci. Lett. 261, 350–366. https://doi.org/10.1016/j.epsl.2007.06.032.
Li, W., Mu, G., Zhang, W., Lin, Y., Zhang, D., Song, H., 2019. Formation of greigite (Fe_3S_4) in the sediments of saline Lake Lop Nur, Northwest China, and its implications for paleo-environmental change during the last 8400 years. J. Asian Earth Sci. 174, 99–108. https://doi.org/10.1016/j.jseaes.2018.11.021.
Liu, J., Zhu, R., Roberts, A.P., Li, S., Chang, J.-H., 2004. High-resolution analysis of early diagenetic effects on magnetic minerals in post-middle-Holocene continental shelf sediments from the Korea Strait. J. Geophys. Res. Solid Earth 109, B03103. https://doi.org/10.1029/2003JB002813.
Liu, J., Shi, X., Liu, Q., Liu, S., Liu, Y., Zhang, Q., Yu, X., Fang, X., Wu, Y., Xu, T., Li, J., 2021. Authigenic Iron sulfides Indicate Sea-level change on the continental shelf: An illustration from the East China Sea. J. Geophys. Res. Solid Earth 126. https://doi.org/10.1029/2020JB021222.
Lucifora, S., Cifelli, F., Mattei, M., Sagnotti, L., Cosentino, D., Roberts, A.P., 2012. Inconsistent magnetic polarities in magnetite- and greigite-bearing sediments: understanding complex magnetizations in the late Messinian in the Adana Basin (southern Turkey). Geochem. Geophys. Geosyst. 13, Q10002. https://doi.org/10.1029/2012GC004248.
Ludwig, P., Egli, R., Bishop, S., Chernenko, V., Frederichs, T., Rugel, G., Merchel, S., Orgeira, M.J., 2013. Characterization of primary and secondary magnetite in marine sediment by combining chemical and magnetic unmixing techniques. Glob. Planet. Chang. 210, 321–339. https://doi.org/10.1016/j.gloplacha. 2013.08.018.
Mach, K., Teodoridis, V., Grygar, T.M., Kvaek, Z., Suhr, P., Standke, G., 2014. An evaluation of palaeogeography and palaeoecology in the Most Basin (Czech Republic) and Saxony (Germany) from the late Oligocene to the early Miocene. Neues Jahrb. Geol. Palaontol. Abh. 272, 13–45. https://doi.org/10.1127/0077-7749/2014/0395.
Mach, K., Rapprich, V., Faměra, M., Havelcová, M., Matys Grygar, T., Novotný, T., Řehoř, M., Kochergina, Y.E., 2021. Crandallite-rich beds of the Libkovice member, Most Basin, Czech Republic: climatic extremes or paleogeographic changes at the onset of the Miocene climatic optimum? Geol. Acta 19, 1–29. https://doi.org/10.1344/GeologicaActa2021.19.11.
Maffione, M., Herrero-Bervera, E., 2022. A relative Paleointensity (RPI)-calibrated age model for the Corinth Syn-rift sequence at IODP hole M0079A (gulf of Corinth, Greece). Front. Earth Sci. 10, 813958 https://doi.org/10.3389/feart.2022.813958.
Mandic, O., Rundić, L., Ćorić, S., Pezelj, Đ., Theobalt, D., Sant, K., Krijgsman, W., 2019. Age and mode of the middle Miocene marine flooding of the Pannonian basin—constraints from Central Serbia. Palaios 34, 71–95. https://doi.org/10.2110/palo.2018.052.
Márton, E., Pipík, R., Starek, D., Kovácsi, E., Vidhya, M., Świerczewska, A., Tokarski, A. K., Vojtko, R., Schlögl, S., 2022. Enhancing the reliability of the magnetostratigraphic age assignment of azimuthally nonoriented drill cores by the integrated application of palaeomagnetic analysis, field tests, anisotropy of magnetic susceptibility, and the evolution of the endemic fauna as documented on the upper Miocene limnic deposits of the Turiec Basin (Western Carpathians). AAPG Bull. 106, 803–827. https://doi.org/10.1306/10042120019.
Matys Grygar, T., Mach, K., 2013. Regional chemostratigraphic key horizons in the macrofossil-barren siliciclastic lower Miocene lacustrine sediments (Most Basin, Eger graben, Czech Republic). Bull. Geosci. 557–571 https://doi.org/10.3140/bull.geosci.1372.
Matys Grygar, T., Mach, K., Schnabl, P., Pruner, P., Laurin, J., Martinez, M., 2014. A lacustrine record of the early stage of the Miocene climatic optimum in Central Europe from the Most Basin, Ohře (Eger) graben, Czech Republic. Geol. Mag. 151, 1013–1033. https://doi.org/10.1017/S0016756813001052.
Matys Grygar, T., Hošek, M., Mach, K., Schnabl, P., Martinez, M., 2017a. Climatic instability before the Miocene climatic optimum reflected in a central European lacustrine record from the Most Basin in the Czech Republic. Palaeogeogr. Palaeoclimatol. Palaeoecol. 485, 930–945. https://doi.org/10.1016/j.palaeo.2017.08.011.
Matys Grygar, T., Mach, K., Hošek, M., Schnabl, P., Martinez, M., Koubová, M., 2017b. Early stages of clastic deposition in the Most Basin (Ohře rift, Czech Republic, early Miocene): timing and possible controls. Bull. Geosci. 92, 337–355. https://doi.org/10.3140/bull.geosci.1656.
Matys Grygar, T., Mach, K., Schnabl, P., Martinez, M., Zeeden, C., 2019. Orbital forcing and abrupt events in a continental weathering proxy from Central Europe (Most Basin, Czech Republic, 17.7–15.9 ma) recorded beginning of the Miocene climatic optimum. Palaeogeogr. Palaeoclimatol. Palaeoecol. 514, 423–440. https://doi.org/10.1016/j.palaeo.2018.10.034.
Matys Grygar, T., Mach, K., Koubová, M., Martinez, M., Hron, K., Fačevicová, K., 2021. Beginning of the Miocene climatic optimum in Central Europe in sediment archive of the Most Basin, Czech Republic. Bull. Geosci. 61–81 https://doi.org/10.3140/bull.geosci.1794.
Maxbauer, D.P., Feinberg, J.M., Fox, D.L., 2016. MAX UnMix: a web application for unmixing magnetic coercivity distributions. Comput. Geosci. 95, 140–145. https://doi.org/10.1016/j.cageo.2016.07.009.
McElhinny, M.W., McFadden, P.L., 1999. Paleomagnetism: Continents and Oceans. Elsevier.
McElhinny, M.W., McFadden, P.L., Merrill, R.T., 1996. The time-averaged paleomagnetic field 0–5 Ma. J. Geophys. Res. Solid Earth 101 (B11), 25007–25027. https://doi.org/10.1029/96JB01911.
McFadden, P.L., Reid, A.B., 1982. Analysis of palaeomagnetic inclination data. Geophys. J. Int. 69, 307–319. https://doi.org/10.1111/j.1365-246X.1982.tb04950.x.
Mikuláš, R., Mach, K., Dvořák, Z., 2003. Bioturbation of claystones of the Most Basin in the Bílina quarry (Miocene, Czech Republic). Acta Univ. Carol. Geol. 47, 79–85.
Musgrave, R.J., Kars, M., 2016. Recognizing magnetostratigraphy in overprinted and altered marine sediments: challenges and solutions from IODP site U1437. Geochem. Geophys. Geosyst. 17, 3190–3206. https://doi.org/10.1002/2016GC006386.
Muxworthy, A.R., Williams, W., 2009. Critical superparamagnetic/single-domain grain sizes in interacting magnetite particles: implications for magnetosome crystals. J. R. Soc. Interface 6, 1207–1212. https://doi.org/10.1098/rsif.2008.462.
Muxworthy, A.R., Williams, W., Roberts, A.P., Winklhofer, M., Chang, L., Pósfai, M., 2013. Critical single domain grain sizes in chains of interacting greigite particles: implications for magnetosome crystals. Geochem. Geophys. Geosyst. 14, 5430–5441. https://doi.org/10.1002/2013GC004973.
Nowaczyk, N.R., Arz, H.W., Frank, U., Kind, J., Plessen, B., 2012. Dynamics of the Laschamp geomagnetic excursion from Black Sea sediments. Earth Planet. Sci. Lett. 351–352, 54–69. https://doi.org/10.1016/j.epsl.2012.06.050.
Nowaczyk, N.R., Liu, J., Arz, H.W., 2021. Records of the Laschamps geomagnetic polarity excursion from Black Sea sediments: magnetite versus greigite, discrete sample versus U-channel data. Geophys. J. Int. 224 (2), 1079–1095. https://doi.org/10.1093/gji/ggaa506.
Ogg, J.G., 2020. Geomagnetic polarity time scale. In: Geologic Time Scale, 2020. Elsevier, pp. 159–192. https://doi.org/10.1016/B978-0-12-824360-2.00005-X.

Ohneiser, C., Beltran, C., Bollen, M., Fougere, D., Egli, R., 2024. Interdecadal Pacific oscillation modulation of Western Pacific climate during the Holocene. Nat. Commun. (under revision).

O'Reilly, W., Hoffmann, V., Chouker, A.C., Soffel, H.C., Menyeh, A., 2000. Magnetic properties of synthetic analogues of pyrrhotite ore in the grain size range 1-24 μm. Geophys. J. Int. 142, 669–683. https://doi.org/10.1046/j.1365-246x.2000.00169.x.

Ouyang, T., Heslop, D., Roberts, A.P., Tian, C., Zhu, Z., Qiu, Y., Peng, X., 2014. Variable remanence acquisition efficiency in sediments containing biogenic and detrital magnetites: implications for relatve paleointensity signal recording. Geochem. Geophys. Geosyst. 15, 2780–2796. https://doi.org/10.1002/2014GC005301.

Özdemir, Ö., Dunlop, D.J., Moskowitz, B.M., 1993. The effect of oxidation on the Verwey transition in magnetite. Geophys. Res. Lett. 20, 1671–1674. https://doi.org/10.1029/93GL01483.

Paterson, G.A., Zhao, X., Jackson, M., Heslop, D., 2018. Measuring, processing, and analyzing hysteresis data. Geochem. Geophys. Geosyst. 19, 1925–1945. https://doi.org/10.1029/2018GC007620.

Pick, T., Tauxe, L., 1991. Chemical remanent magnetiation in synthetic magnetite. J. Geophys. Res. 96, 9925–9936. https://doi.org/10.1029/91JB00706.

Pick, T., Tauxe, L., 1993. Holocene paleointensities: Thellier experiments on submarine basaltic glass from the East Pacific rise. J. Geophys. Res. 98, 17949–17964. https://doi.org/10.1029/93JB01160.

Pike, C.R., Roberts, A.P., Verosub, K.L., 2001. First-order reversal curve diagrams and thermal relaxation in magnetic particles. Geophys. J. Int. 145, 721–730. https://doi.org/10.1046/j.0956-540x.2001.01419.x.

Potter, D.K., Stephenson, A., 2005. New observations and theory of single-domain magnetic moments. J. Phys. Conf. Ser. 17, 168–173. https://doi.org/10.1088/1742-6596/17/1/023.

Potter, D.K., Ali, A., Abdalah, S., 2019. Templates for quantifying clay type and clay content from magnetic susceptibility and standard borehole geophysical measurements. J. Mod. Phys. 10, 824–834. https://doi.org/10.4236/jmp.2019.107055.

Rajchl, M., Uličný, D., Mach, K., 2008. Interplay between tectonics and compaction in a rift-margin, lacustrine delta system: Miocene of the Eger graben, Czech Republic: Tectonics and compaction in a rift-margin delta. Sedimentology 55, 1419–1447. https://doi.org/10.1111/j.1365-3091.2008.00951.x.

Rajchl, M., Uličný, D., Grygar, R., Mach, K., 2009. Evolution of basin architecture in an incipient continental rift: the Cenozoic Most Basin, Eger graben (Central Europe). Basin Res. 21, 269–294. https://doi.org/10.1111/j.1365-2117.2008.00393.x.

Roberts, A.P., 1995. Magnetic properties of sedimentary greigite (Fe_3S_4). Earth Planet. Sci. Lett. 134, 227–236. https://doi.org/10.1016/0012-821X(95)00131-U.

Roberts, A.P., Weaver, R., 2005. Multiple mechanisms of remagnetization involving sedimentary greigite (Fe_3S_4). Earth Planet. Sci. Lett. 231, 263–277. https://doi.org/10.1016/j.epsl.2004.11.024.

Roberts, A.P., Reynolds, R.L., Verosub, K.L., Adam, D.P., 1996. Environmental magnetic implications of Greigite (Fe_3S_4) formation in a 3 m.y. lake sediment record from Butte Valley, northern California. Geophys. Res. Lett. 23, 2859–2862. https://doi.org/10.1029/96GL02831.

Roberts, A.P., Liu, Q., Rowan, C.J., Chang, L., Carvallo, C., Torrent, J., Horng, C.-S., 2006. Using first-order reversal curve diagrams. J. Geophys. Res. Solid Earth 111. https://doi.org/10.1029/2006JB004715. B12S35. Characterization of hematite (α-Fe2O3), goethite (α -FeOOH), greigite (Fe3S4), and pyrrhotite (Fe7S8).

Roberts, A.P., Chang, L., Rowan, C.J., Horng, C.-S., Florindo, F., 2011. Magnetic properties of sedimentary greigite (Fe_3S_4): An update. Rev. Geophys. 49 https://doi.org/10.1029/2010RG000336. RG1002.

Roberts, A.P., Almeida, T.P., Church, N.S., Harrison, R.J., Heslop, D., Li, Y., Li, J., Muxworthy, A.R., Williams, W., Zhao, X., 2017. Resolving the origin of pseudo-single domain magnetic behavior. J. Geophys. Res. Solid Earth 122, 9534–9558. https://doi.org/10.1002/2017JB014860.

Roberts, A.P., Tauxe, L., Heslop, D., Zhao, X., Jiang, Z., 2018. A critical appraisal of the "Day" diagram. J. Geophys. Res. 123, 2618–2644. https://doi.org/10.1002/2017JB015247.

Roberts, A.P., Hu, P., Harrison, R.J., Heslop, D., Muxworthy, A.R., Oda, H., Sato, T., Tauxe, L., Zhao, X., 2019. Domain state diagnosis in rock magnetism: evaluation of potential alternatives to the Day diagram. J. Geophys. Res. Solid Earth 124 (6), 5286–5314. https://doi.org/10.1029/2018JB017049.

Roud, S., Gilder, S.A., SoHyun, P., 2022. Greigite (Fe_3S_4) formation in artificial sediments via solid- state transformation of lepidocrocite. Geochem. Geophys. Geosyst. 23 https://doi.org/10.1029/2022GC010376 e2022GC010376.

Rowan, C.J., Roberts, A.P., 2006. Magnetite dissolution, diachronous greigite formation, and secondary magnetizations from pyrite oxidation: unravelling complex magnetizations in Neogene marine sediments from New Zealand. Earth Planet. Sci. Lett. 241, 119–137. https://doi.org/10.1016/j.epsl.2005.10.017.

Rowan, C.J., Roberts, A.P., Broadbent, T., 2009. Reductive diagenesis, magnetite dissolution, greigite growth and paleomagnetic smoothing in marine sediments: a new view. Earth Planet. Sci. Lett. 277, 223–235. https://doi.org/10.1016/j.epsl.2008.10.016.

Sagnotti, L., Winkler, A., 1999. Rock magnetism and palaeomagnetism of greigite-bearing mudstones in the Italian peninsula. Earth Planet. Sci. Lett. 165, 67–80. https://doi.org/10.1016/S0012-821X(98)00248-9.

Sagnotti, L., Roberts, A.P., Weaver, R., Verosub, K.L., Florindo, F., Pike, C.R., Clayton, T., Wilson, G.S., 2005. Apparent magnetic polarity reversals due to remagnetization resulting from late diagenetic growth of greigite from siderite. Geophys. J. Int. 160, 89–100. https://doi.org/10.1111/j.1365-246X.2005.02485.x.

Scheidt, S., Egli, R., Frederichs, T., Hambach, U., Rolf, C., 2017. A mineral magnetic characterization of the Plio-Pleistocene fluvial infill of the Heidelberg Basin (Germany). Geophys. J. Int. 210, 743–764. https://doi.org/10.1093/gji/ggx154.

Scheidt, S., Egli, R., Lenz, M., Rolf, C., Fabian, K., Melles, M., 2021. Mineral magnetic characterization of high-latitude sediments from Lake Levinson-Lessing, Siberia. Geophys. Res. Lett. 48 (10) https://doi.org/10.1029/2021GL093026 e2021GL093026.

Schneider, D.A., Kent, D.V., 1988. Inclination anomalies from Indian Ocean sediments and the possibility of a standing nondipole field. J. Geophys. Res. 93, 11621. https://doi.org/10.1029/JB093iB10p11621.

Sier, M.J., Langereis, C.G., Dupont-Nivet, G., Feibel, C.S., Joordens, J.C.A., van der Lubbe, J.H.J.L., Beck, C.C., Olago, D., Cohen, A., 2017. The top of the Olduvai Subchron in a high-resolution magnetostratigraphy from the West Turkana core WTK13, hominin sites and Paleolakes drilling project (HSPDP). Quat. Geochronol. 42, 117–129. https://doi.org/10.1016/j.quageo.2017.08.004.

Snowball, I.F., 1997a. Gyroremanent magnetization and the magnetic properties of greigite-bearing clays in southern Sweden. Geophys. J. Int. 129, 624–636. https://doi.org/10.1111/j.1365-246X.1997.tb04498.x.

Snowball, I.F., 1997b. The detection of single-domain greigite (Fe_3S_4) using rotational remanent magnetization (RRM) and the effective gyro field (Bg): mineral magnetic and palaeomagnetic applications. Geophys. J. Int. 130, 704–716. https://doi.org/10.1111/j.1365-246X.1997.tb01865.x.

Snowball, I., Thompson, R., 1990. A stable chemical remanence in Holocene sediments. J. Geophys. Res. 95, 4471. https://doi.org/10.1029/JB095iB04p04471.

Snowball, I., Almqvist, B., Lougheed, B.C., Wiers, S., Obrochta, S., Herrero-Bervera, E., 2019. Coring induced sediment fabrics at IODP expedition 347 sites M0061 and M0062 identified by anisotropy of magnetic susceptibility (AMS): criteria for accepting palaeomagnetic data. Geophys. J. Int. 217, 1089–1107. https://doi.org/10.1093/gji/ggz075.

Spender, M.R., Coey, J.M.D., Morrish, A.H., 1972. The magnetic properties and Mössbauer spectra of synthetic samples of Fe_3S_4. Can. J. Phys. 50, 2313–2326. https://doi.org/10.1139/p72-306.

Stephenson, A., 1993. Three-axis static alternating field demagnetization of rocks and the identification of natural remanent magnetization, gyroremanent magnetization, and anisotropy. J. Geophys. Res. 98, 373–381. https://doi.org/10.1029/92JB01849.

Tarling, D., Hrouda, F., 1993. Magnetic Anisotropy of Rocks. Springer Science & Business Media.

Torii, M., Fukuma, K., Horng, C.-S., Lee, T.-Q., 1996. Magnetic discrimination of pyrrhotite- and greigite-bearing sediment samples. Geophys. Res. Lett. 23, 1813–1816. https://doi.org/10.1029/96GL01626.

Ucar, H., Kletetschka, G., Kadlec, J., 2021. Evidence of the Matuyama-Brunhes transition in cave sediment in Central Europe. Quat. Int. 604, 16–27. https://doi.org/10.1016/j.quaint.2021.07.005.

Vasiliev, I., Dekkers, M.J., Krijgsman, W., Franke, C., Langereis, C.G., Mullender, T.A.T., 2007. Early diagenetic greigite as a recorder of the palaeomagnetic signal in Miocene-Pliocene sedimentary rocks of the Carpathian foredeep (Romania). Geophys. J. Int. 171, 613–629. https://doi.org/10.1111/j.1365-246X.2007.03560.x.

Vasiliev, I., Franke, C., Meeldijk, J.D., Dekkers, M.J., Langereis, C.G., Krijgsman, W., 2008. Putative greigite magnetofossils from the Pliocene epoch. Nat. Geosci. 1, 782–786.

Wagner, C.L., Egli, R., Lascu, I., Lippert, P.C., Livi, K.J.T., Sears, H.B., 2021. In-situ identification of giant, needle-shaped magnetofossils in Paleocene-Eocene thermal maximum sediments. Proc. Nat. Acad. Sci. United States (PNAS) 118, e2018169118. https://doi.org/10.1073/pnas.2018169118.

Weaver, R., Roberts, A.P., Barker, A.J., 2002. A late diagenetic (syn-folding) magnetization carried by pyrrhotite: implications for paleomagnetic studies from magnetic iron sulphide-bearing sediments. Earth Planet. Sci. Lett. 200, 371–386. https://doi.org/10.1016/S0012-821X(02)00652-0.

Worm, H.-U., 1998. On the superparamagnetic-stable single domain transition for magnetite, and frequency dependence of susceptibility. Geophys. J. Int. 133, 201–206. https://doi.org/10.1046/j.1365-246X.1998.1331468.x.

Yang, T., Zhao, X., Petronotis, K., Dekkers, M.J., Xu, H., 2019. Anisotropy of magnetic susceptibility (AMS) of sediments from holes U1480E and U1480H, IODP expedition 362: sedimentary or artificial origin and implications for Paleomagnetic studies. Geochem. Geophys. Geosyst. 20, 5192–5215. https://doi.org/10.1029/2019GC008721.

Zijderveld, J.D., 1967. A. C. Demagnetization of rocks. In: Collinson, D.W., Creer, K.M., Runcorn, S.K. (Eds.), Methods in Palaeomagnetism. Elsevier, Amsterdam, pp. 254–286.